Petroleum Science 20 (2023) 2092–2112

Contents lists available at ScienceDirect

Petroleum Science

journal homepage: www.keaipublishing.com/en/journals/petroleum-science

Original Paper

Rock physics and seismic reflectivity parameterization and amplitude variation with offsets inversion in terms of total organic carbon indicator

Song-He Yu [a, b, c], Zhao-Yun Zong [a, b, c, *], Xing-Yao Yin [a, b, c], Kun Lang [a, b, c], Fu-Bin Chen [a, b, c]

[a] School of Geosciences, China University of Petroleum (East China), Qingdao, Shandong, 266580, China
[b] Pilot National Laboratory for Marine Science and Technology (Qingdao), Qingdao, Shandong, 266580, China
[c] Shandong Provincial Key Laboratory of Deep Oil and Gas, Qingdao, Shandong, 266580, China

A R T I C L E I N F O

Article history:
Received 9 August 2022
Received in revised form
28 December 2022
Accepted 15 February 2023
Available online 16 February 2023

Edited by Jie Hao

Keywords:
TOC
Rock physics
Seismic reflectivity
AVO inversion
Source rocks

A B S T R A C T

Total organic carbon (TOC) prediction with elastic parameter inversions has been widely used in the identification and evaluation of source rocks. However, the elastic parameters used to predict TOC are not only determined by TOC but also depend on the other physical properties of source rocks. Besides, the TOC prediction with the elastic parameters inversion is an indirect method based on the statistical relationship obtained from well logs and experiment data. Therefore, we propose a rock physics model and define a TOC indicator mainly affected by TOC to predict TOC directly. The proposed rock physics model makes the equivalent elastic moduli of source rocks parameterized by the TOC indicator. Combining the equivalent elastic moduli of source rocks and Gray's approximation leads to a novel linearized approximation of the P-wave reflection coefficient incorporating the TOC indicator. Model examples illustrate that the novel reflectivity approximation well agrees with the exact Zoeppritz equation until incident angles reach 40°. Convoluting the novel P-wave reflection approximation with seismic wavelets as the forward solver, an AVO inversion method based on the Bayesian theory is proposed to invert the TOC indicator with seismic data. The synthetic examples and field tests validate the feasibility and stability of the proposed AVO inversion approach. Using the inversion results of the TOC indicator, TOC is directly and accurately estimated in the target area.

1. Introduction

Quantifying organic matter abundance, determining organic matter type, and analyzing organic matter maturity are three essential aspects investigated for identifying and evaluating potential source rocks (Herron, 1987). The most popular focus in determining source rocks is how to predict TOC (Herron, 1987; Li et al., 2018; Shalaby et al., 2019). Elastic parameter inversions have been widely used to map the TOC distributions based on the correlation between TOC and its sensitive elastic parameters (such as P-wave velocity, density, and P-wave impedance) (Amato del Monte et al., 2018; Broadhead et al., 2016; Løseth et al., 2011; Sahoo et al., 2021). The widely investigated artificial intelligence technology has also been applied to estimate TOC using different sensitivity parameters (Amosu et al., 2021; Chan et al., 2022; Shalaby et al., 2019; Zhao et al., 2021). However, the elastic parameters used to predict TOC are not only determined by TOC but also affected by other physical parameters of source rocks, such as clay content and porosity. Besides, the TOC prediction with the elastic parameters inversion is an indirect method and includes two main steps: elastic parameters inversion and TOC estimation from elastic parameters. The basis of TOC prediction using elastic parameters is the statistical relationship obtained from well logs and experiment data and lacks inherent rock physics interpretation (Amato del Monte et al., 2018; Sahoo et al., 2021; Zhao et al., 2021). Therefore, we aim to present an effective parameter by rock physics modeling, which mainly depends on TOC and is defined as a TOC

* Corresponding author. School of Geosciences, China University of Petroleum (East China), Qingdao, Shandong, 266580, China.
E-mail address: zongzhaoyun@126.com (Z.-Y. Zong).

https://doi.org/10.1016/j.petsci.2023.02.012

indicator for directly predicting TOC.

Extensive investigations have focused on the rock physics of source rocks in recent years. Vernik and Nur (1992) first revealed that kerogen has a noticeable impact on the seismic velocities of shale by ultrasonic measurement. Subsequently, many geophysicists paid attention to the effects of kerogen on the elastic responses of source rocks or shale (Carcione, 2000; Fu et al., 2020; Hansen et al., 2019; Zhao et al., 2016). The typical effective medium theories for simulating the elastic responses of kerogen on source rocks or shale include Backus averaging theory and its modifications (Backus, 1962; Carcione, 2000; Sayers, 2013; Vernik and Landis, 1996; Vernik and Liu, 1997; Vernik and Nur, 1992; Zhao et al., 2016), Kuster-Toksöz (K-T) model (Han et al., 2019; Kuster and Toksöz, 1974), isotropic and anisotropic SCA model (Berryman, 1980, 1995; Li et al., 2015; Yin et al., 2020; Yu et al., 2021), isotropic DEM and anisotropy DEM model (Deng et al., 2015; Hornby et al., 1994), anisotropy SCA-DEM model (Gui et al., 2020; Hornby et al., 1994), solid substitution equation (Fu et al., 2020; Saxena and Mavko, 2014; Yu et al., 2021; Zhao et al., 2016), Brown-Korringa equation(Brown and Korringa, 1975; Dong et al., 2014; Yin et al., 2020), and anisotropic generalization of Gassmann equations (Carcione and Avseth, 2015; Carcione et al., 2011; Ciz and Shapiro, 2009). The selection and usage of effective models depend on the elastic properties and mechanical effects of kerogen. For example, the Backus average, K-T model, SCA model, and DEM model are typically used in the case that kerogen is regarded as a prominent part of the rock matrix and plays the role of loading-bearing. The Brown-Korringa equation, solid substitution equation, and the anisotropic generalization of Gassmann equations will be applied when the kerogen is treated as the inclusion filling of rock pores. As thermal maturation increases, kerogen is gradually converted to hydrocarbon, and kerogen-related pores are generated; besides, the role of kerogen transforms from load bearing to inclusion infilling (Tissot et al., 1974; Zargari et al., 2015; Zhao et al., 2016). Therefore, varied rock physics models may be applied to adapt to the changes in kerogen elastic properties with maturity (Yin et al., 2020; Yu et al., 2021; Zhao et al., 2016). However, using the above rock physics models, the effect of kerogen on the equivalent elastic moduli of source rocks cannot be expressed explicitly by TOC. Therefore, we propose a new modeling idea of “inorganic before organic,” which means the inorganic rock is first constructed, and then the kerogen is added to constitute source rocks. As studied by Xu and White (1995), the K-T model was used to estimate the elastic moduli of the dry rock skeleton. Under the assumption of constant Poisson's ratio of dry rock skeleton, Keys and Xu (2002) simplified the K-T equations for the elastic moduli for dry rock skeleton. The simplified elastic moduli are expressed as the elastic moduli of the rock medium multiplied by the functions related to the rock porosity only. Referring to the studies of Keys and Xu (2002), we apply the K-T model to incorporate the effect of kerogen on source rocks. As a consequence of simplification, the equivalent elastic moduli of source rocks are parameterized by the equivalent moduli of inorganic rock and a parameter. Because this parameter is the function of TOC and is mainly sensitive to TOC, we define it as the TOC indicator for predicting the TOC of source rocks.

The proposed rock physics model builds a quantitative relation between the elastic properties and physical parameters of source rocks (Mavko et al., 2009). Combining the equivalent elastic moduli of source rocks and Gray’s approximation leads to a novel linearized approximation of the P-wave reflection coefficient incorporating the TOC indicator (Gray et al., 1999; Zong and Yin, 2017; Zong et al., 2015). The AVO inversion is a critical application of the novel P-wave reflection coefficient to predict TOC from pre-stack seismic data (Buland and Omre, 2003; Downton, 2005). Convoluting the novel P-wave reflection approximation with seismic wavelets as the forward solver, an AVO inversion method based on the Bayesian theory is proposed to invert the TOC indicator with seismic data (Zong and Yin, 2016; Zong et al., 2015). Using the inversion results of the TOC indicator, the TOC can be predicted directly, thereby identifying the distribution of source rocks.

As known, the elastic characteristics of source rocks are not only affected by the TOC but also depend on the maturity of organic matter, anisotropy properties of rock medium, and mineral composition (Ding et al., 2021; Hansen et al., 2019; Suwannasri et al., 2018; Zhang et al., 2018; Zhao et al., 2016). This paper’s research object is isotropic, low maturity, and clay-rich source rocks.

2. Rock physics parameterization

The rock physics model builds a quantitative relation between the elastic properties and physical parameters of source rocks, and provides crucial theoretical support for the accurate prediction of TOC by seismic inversion (Grana, 2016; Mavko et al., 2009). To decouple the elastic responses of TOC, we first construct inorganic rock and then incorporate kerogen to compose the organic-rich source rock, thereby parameterizing the equivalent elastic moduli of source rocks. Building the rock physics model of source rocks includes four steps. Fig. 1 shows the steps and details of the model.

Step 1. The V-R-H average is applied to calculate the elastic moduli of rock medium mixing different minerals (Hill, 1952; Mavko et al., 2009):

$$M_{\mathrm{m}} = \left[\sum_{i=1}^{N} f_i M_i + \left(\sum_{i=1}^{N} f_i / M_i\right)^{-1}\right] / 2, \tag{1}$$

where, M_{m} and M_i represent the elastic moduli of the rock medium and i th mineral component, respectively. f_i is the volume fraction of the i th mineral component.

Step 2. The pore space is divided into clay pores and sand pores (Xu and White, 1995):

$$\varphi_{\mathrm{clay}} = V_{\mathrm{clay}} \Big/ V_{\mathrm{total}} {*} \varphi_{\mathrm{matrix}},\ \varphi_{\mathrm{sand}} = \varphi_{\mathrm{matrix}} - \varphi_{\mathrm{clay}}, \tag{2}$$

where, $\varphi_{\mathrm{matrix}}$ is the total matrix porosity, φ_{clay} and φ_{sand} are porosities of clay pores and sand pores, respectively.

The simplified equations deduced by Keys and Xu (2002) are used to estimate the elastic moduli of dry rock skeleton:

$$K_{\mathrm{dry}} = K_{\mathrm{m}}(1-\varphi_i)^{p_i}, \tag{3}$$

$$\mu_{\mathrm{dry}} = \mu_{\mathrm{m}}(1-\varphi_i)^{q_i}, \tag{4}$$

where, K_{dry} and μ_{dry} are the bulk modulus and shear modulus of dry rock skeleton, respectively. p_i and q_i are the geometry parameters of matrix pores, which are related to the aspect ratio of inclusion pores and Poisson’s ratio of the minerals.

Step 3. The mixture of pore fluids is calculated by Wood equation (Mavko et al., 2009; Wood, 1955):

$$\frac{1}{K_{\mathrm{f}}} = \sum_{i=1}^{N} \frac{f_i}{K_i}, \tag{5}$$

Gassmann equations are next applied to add the fluid mixture to constitute inorganic rocks. (Gassmann, 1951; Mavko et al., 2009):

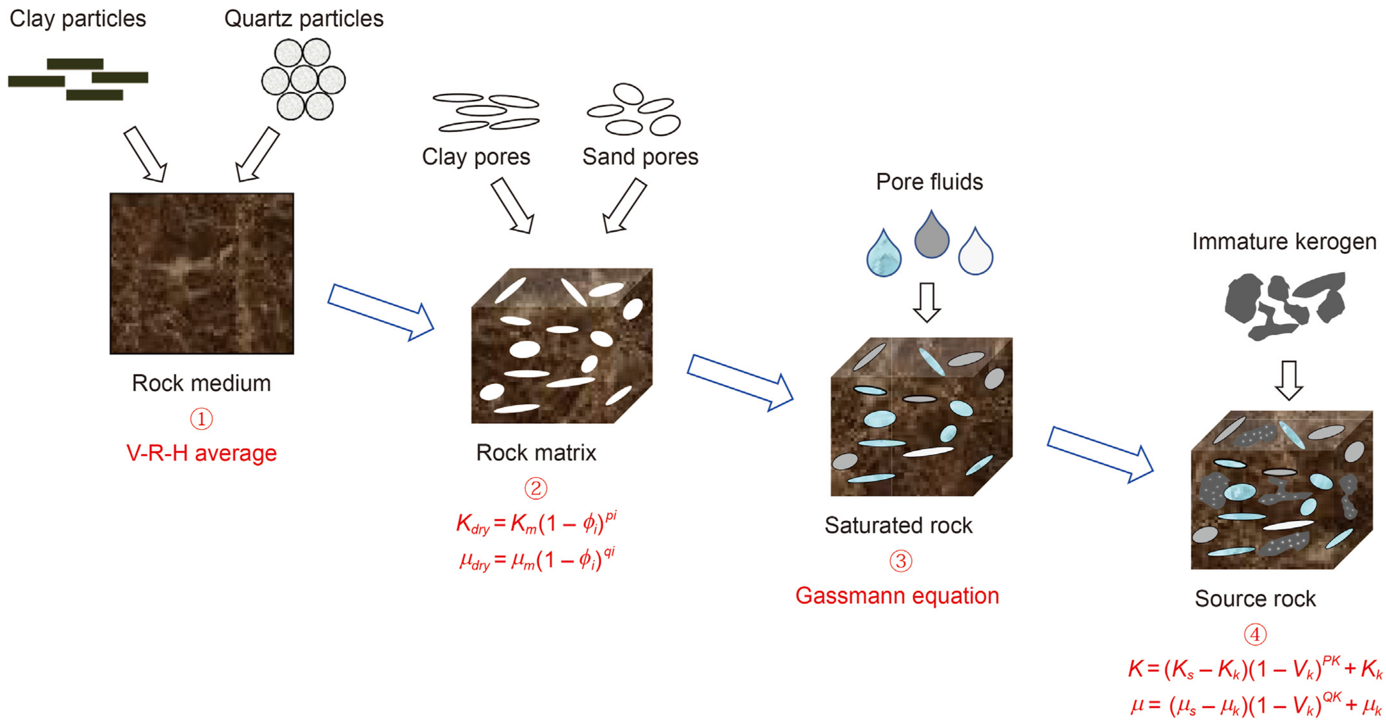

Fig. 1. Modeling methodology and rock physics model of source rocks.

$$K_{\mathrm{s}} = K_{\mathrm{d}} + \frac{(1 - K_{\mathrm{d}}/K_{\mathrm{m}})^2 K_{\mathrm{f}}}{\left[\varphi + (1 - K_{\mathrm{d}}/K_{\mathrm{m}} - \varphi)K_{\mathrm{f}}/K_{\mathrm{m}}\right]}, \tag{6}$$

$$\mu_{\mathrm{s}} = \mu_{\mathrm{d}}, \tag{7}$$

where, K_{s} and μ_{s} are the bulk modulus and shear modulus of the inorganic rock, respectively.

Step 4. The kerogen is finally added to the source rock by the K-T model (Kuster and Toksöz, 1974; Mavko et al., 2009):

$$K - K_{\mathrm{s}} = \frac{(K_{\mathrm{k}} - K_{\mathrm{s}})}{3} \frac{3K + 4\mu_{\mathrm{s}}}{3K_{\mathrm{s}} + 4\mu_{\mathrm{s}}} \cdot V_{\mathrm{k}} T_{iijj}(\alpha_{\mathrm{k}}), \tag{8}$$

$$\mu - \mu_{\mathrm{s}} = \frac{(\mu_{\mathrm{k}} - \mu_{\mathrm{s}})}{5} \frac{6\mu(K_{\mathrm{s}} + 2\mu_{\mathrm{s}}) + \mu_{\mathrm{s}}(9K_{\mathrm{s}} + 8\mu_{\mathrm{s}})}{5\mu_{\mathrm{s}}(3K_{\mathrm{s}} + 4\mu_{\mathrm{s}})} \cdot V_{\mathrm{k}} F(\alpha_{\mathrm{k}}), \tag{9}$$

where, K and μ are the equivalent elastic moduli of source rocks. K_{k} and μ_{k} are the elastic moduli of the kerogen. V_{k} represents the volume fraction of kerogen and is related to the TOC. $T_{iijj}(\alpha_{\mathrm{k}})$ and $F(\alpha_{\mathrm{k}})$ are the functions of the kerogen aspect ratio, the equations of $T_{iijj}(\alpha_{\mathrm{k}})$ and $F(\alpha_{\mathrm{k}})$ are given in Appendix A.

The requirement of the K-T equations is $V_i/\alpha \ll 1$. Namely, the ratio of added volume to the kerogen aspect ratio is minimal. Therefore, the kerogen is divided into lots of portions satisfying the condition of the K-T model and added to the source rock iteratively. At each iteration, let $K(V_{\mathrm{k}})$ and $K(V_{\mathrm{k}} + \mathrm{d}V_{\mathrm{k}})$ represent the effective bulk moduli of source rock as the kerogen volume fraction are V_{k} and $V_{\mathrm{k}} + \mathrm{d}V_{\mathrm{k}}$, respectively. When the kerogen volume fraction is V_{k}, $K(V_{\mathrm{k}})$ can be regarded as K_{s}, and $K(V_{\mathrm{k}} + \mathrm{d}V_{\mathrm{k}})$ replaces K in Eq. (8). Similarly, $\mu(V_{\mathrm{k}})$ and $\mu(V_{\mathrm{k}} + \mathrm{d}V_{\mathrm{k}})$ replace μ_{s} and μ in Eq. (9), respectively. Then, Eq. (8) and Eq. (9) equal to

$$K(V_{\mathrm{k}} + \mathrm{d}V_{\mathrm{k}}) - K(V_{\mathrm{k}}) = \frac{[K_{\mathrm{k}} - K(V_{\mathrm{k}})]}{3} \frac{3K(V_{\mathrm{k}} + \mathrm{d}V_{\mathrm{k}}) + 4\mu(V_{\mathrm{k}})}{3K(V_{\mathrm{k}}) + 4\mu(V_{\mathrm{k}})} \cdot V_{\mathrm{k}} T_{iijj}(\alpha_{\mathrm{k}}), \tag{10}$$

$$\mu(V_{\mathrm{k}} + \mathrm{d}V_{\mathrm{k}}) - \mu(V_{\mathrm{k}}) = \frac{[\mu_{\mathrm{k}} - \mu(V_{\mathrm{k}})]}{5} \frac{6\mu(V_{\mathrm{k}} + \mathrm{d}V_{\mathrm{k}})[K(V_{\mathrm{k}}) + 2\mu(V_{\mathrm{k}})] + \mu(V_{\mathrm{k}})[9K(V_{\mathrm{k}}) + 8\mu(V_{\mathrm{k}})]}{5\mu(V_{\mathrm{k}})[3K(V_{\mathrm{k}}) + 4\mu(V_{\mathrm{k}})]} \cdot V_{\mathrm{k}} F(\alpha_{\mathrm{k}}), \tag{11}$$

If $\mathrm{d}V_{\mathrm{k}}$ is allowed to go to zero, then Eq. (10) and Eq. (11) converge to

$$(1 - V_{\mathrm{k}}) \frac{\mathrm{d}K}{\mathrm{d}V_{\mathrm{k}}} = \frac{1}{3}(K_{\mathrm{k}} - K) \cdot V_{\mathrm{k}} T_{iijj}(\alpha_{\mathrm{k}}), \tag{12}$$

$$(1 - V_{\mathrm{k}}) \frac{\mathrm{d}\mu}{\mathrm{d}V_{\mathrm{k}}} = \frac{1}{5}(\mu_{\mathrm{k}} - \mu) \cdot V_{\mathrm{k}} F(\alpha_{\mathrm{k}}), \tag{13}$$

Define a set of "coefficients" P_{k}, Q_{k} and assume that the Poisson's ratio and aspect ratio of kerogen are constants:

$$P_k = \frac{1}{3}V_k T_{iijj}(\alpha_k), \tag{14}$$

$$Q_k = \frac{1}{5}V_k F(\alpha_k), \tag{15}$$

Then for the source rock, Eq. (12) and Eq. (13) are simplified as

$$(1 - V_k)\frac{dK}{dV_k} = (K_k - K)P_k, \tag{16}$$

$$(1 - V_k)\frac{d\mu}{dV_k} = (\mu_k - \mu)Q_k, \tag{17}$$

Because $1 - V_k$ is not zero in source rocks, multiplying both sides of Eq. (16) by $(1 - V_k)^{-1}$ yields

$$\frac{dK}{dV_k} + \frac{P_k}{(1 - V_k)}K = \frac{K_k P_k}{(1 - V_k)}, \tag{18}$$

Eq. (18) is an ordinary differential equation, and its general solution is:

$$\begin{aligned} K &= Ce^{-\int \frac{P_k}{1 - V_k}dV_k} \\ &\quad + e^{-\int \frac{P_k}{1 - V_k}dV_k} \cdot \int \left(\frac{K_k P_k}{1 - V_k} \cdot e^{\int \frac{P_k}{1 - V_k}dV_k}\right)dV_k \\ &= (C_1 + C_2 K_k P_k)(1 - V_k)^{P_k} + K_k, \end{aligned} \tag{19}$$

Since $V_k = 0$, the equivalent bulk modulus of source rocks is the inorganic rock bulk modulus ($K = K_s$), and as $K_k = 0$, the equivalent bulk modulus of source rocks equal to add V_k dry pores to inorganic rock ($K = K_s(1 - V_k)^{P_k}$). Thus, the constants C_1 and C_2 are determined as:

$$\begin{aligned} C_1 &= K_s, \\ C_2 &= -\frac{1}{P_k}, \end{aligned} \tag{20}$$

Finally, the equivalent bulk modulus of source rock is simplified as:

$$K = (K_s - K_k)(1 - V_k)^{P_k} + K_k \tag{21}$$

Similarly, the equivalent shear modulus of source rock is given as:

$$\mu = (\mu_s - \mu_k)(1 - V_k)^{Q_k} + \mu_k \tag{22}$$

The volume fraction of kerogen (V_k) can be converted by TOC, as follows:

$$V_k = \frac{\rho_{rock}}{C_0 \rho_{kerogen}}TOC \tag{23}$$

TOC is one of the most commonly used parameters for evaluating and determining source rocks and can be measured by Rock-Eval. Based on Eq. (21) and Eq. (23), the equivalent elastic moduli of source rocks can be parameterized with inorganic term and TOC term as follow:

$$K = (K_s - K_k)\left(1 - \frac{\rho_{rock}}{C_0\rho_{kerogen}}TOC\right)^{P_k} + K_k = K^E {F_{TOC}}^{P_k} + K_k, \tag{24}$$

$$\mu = (\mu_s - \mu_k)\left(1 - \frac{\rho_{rock}}{C_0\rho_{kerogen}}TOC\right)^{Q_k} + \mu_k = \mu^E {F_{TOC}}^{Q_k} + \mu_k, \tag{25}$$

where, $K^E = K_s - K_k$ represent the equivalent bulk modulus of inorganic rock, $\mu^E = \mu_s - \mu_k$ represent the equivalent shear modulus of inorganic rock, $F_{TOC} = \left(1 - \frac{\rho_{rock}}{C_0\rho_{kerogen}}TOC\right)$ is defined as TOC indicator and represents the elastic effect of TOC on source rock.

The modeling order will directly affect the accuracy of the rock physics model (Mavko et al., 2009). A theoretical model (shown in Table 1) is set to compare the elastic parameters calculated by the "inorganic before organic" and traditional modeling order. Fig. 2 shows that the elastic moduli and velocities of different modeling orders are consistent at the same TOC and fixed clay content, suggesting the feasibility and reliability of the "inorganic before organic" modeling order for the rock physics model of source rocks.

The proposed rock physics model's accuracy will directly affect the inversion results' reliability (Grana, 2016; Mavko et al., 2009). Due to the lack of laboratory experiments on source rock samples, the actual logs of well-A, well-B, and well-C from source rocks in southern China are applied to verify the proposed rock physics model (Xu and Payne, 2009). The interpreted properties of actual well-A, well-B, and well-C (including clay content, TOC, porosity, and water saturation) are shown in Figs. 3–5. The TOC curves of well-A, well-B, and well-C are calculated using the resistivity log, sonic log, Gamma Ray log, and density log by the combination-four-parameter regression method proposed in Yu et al. (2021). Figs. 3–5 show that the predicted elastic velocities agree well with the measured data, and the predicted errors are mainly in the 10% interval. The application results of actual well-A, well-B, and well-C confirm the accuracy and applicability of the proposed rock physics model. The proposed rock physics model can be used to reliably delineate the elastic characteristics of source rocks and be applied to subsequent applications.

The proposed rock physics model illustrates the variations of the equivalent bulk modulus of inorganic rock (K^E), the equivalent shear modulus of inorganic rock (μ^E), and the TOC indicator (F_{TOC}) with TOC (from 0 to 10%) and clay content (from 0 to 100%). From Fig. 6, we can see that the equivalent bulk modulus and shear modulus of inorganic rock (K^E and μ^E) only vary with clay content, and the TOC indicator (F_{TOC}) mainly changes with TOC. Simulation

Table 1
The elastic parameters of the components in the theoretical model.

Component	Bulk modulus, GPa	Shear modulus, GPa	Density, g·cm^{-3}	Sources
Quartz	37.0	44.0	2.65	Carmichael (2017)
Clay	21.0	7.0	2.60	Tosaya and Nur (1982)
kerogen	5.0	3.5	1.26	Zhao et al. (2016)
Water	2.5	0	1.03	Mavko et al. (2009)
Oil	1.08	0	0.80	Mavko et al. (2009)

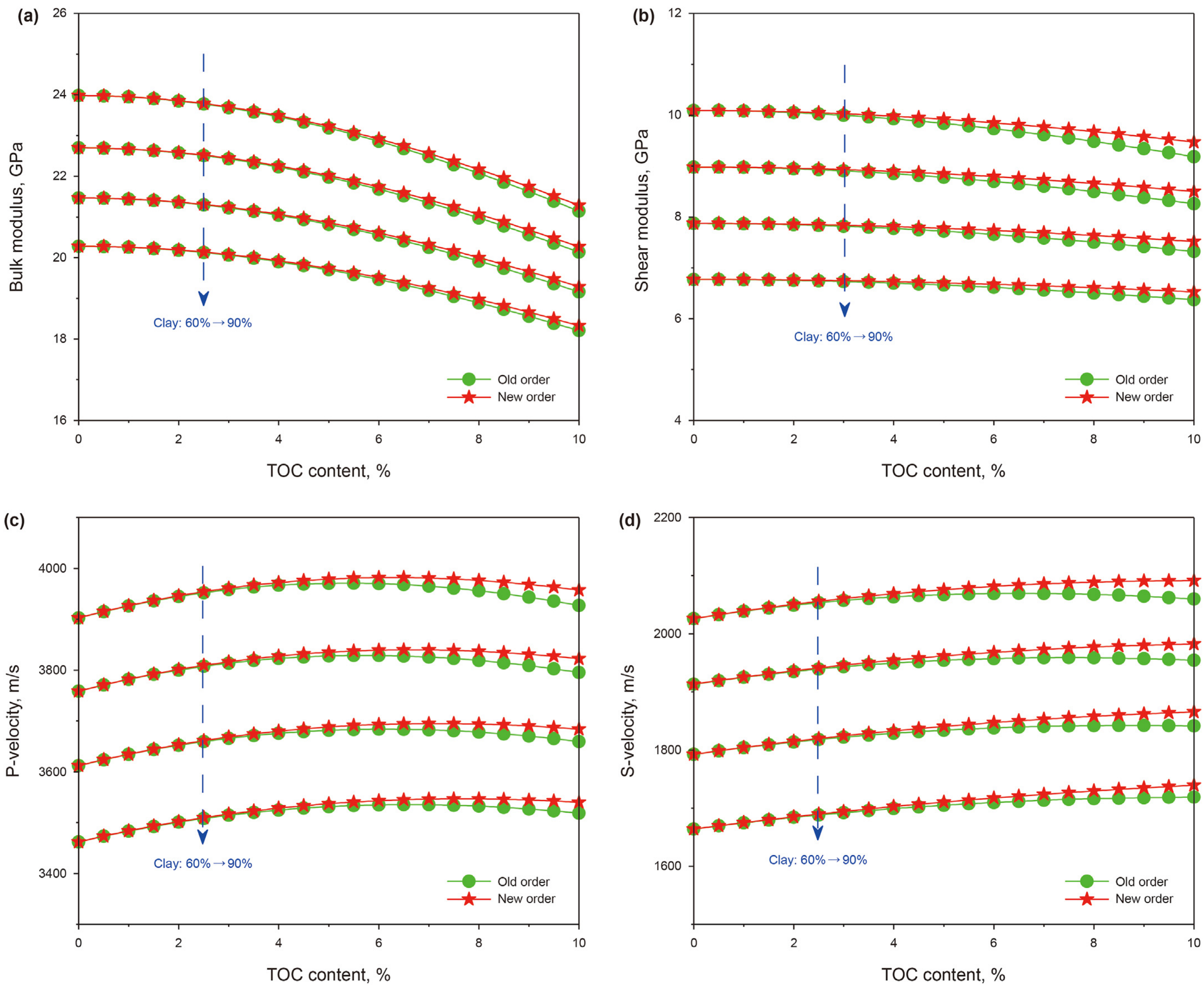

Fig. 2. Comparative results of two modeling orders. (a) Bulk modulus, (b) shear modulus, (c) P-wave velocity, (d) S-wave velocity.

results suggest that the equivalent elastic moduli of inorganic rock (K^E and μ^E) are entirely sensitive to clay content, and the TOC indicator (F_{TOC}) is mainly sensitive to TOC. Thus, we can predict TOC directly using the inversion results of the TOC indicator (F_{TOC}).

Two aspects are considered in the building of the rock physics model. One is the accuracy of the rock physics model, and the other is the feasibility of the rock physics model in seismic reflectivity parameterization and TOC prediction with AVO inversion. Although the result differences between the proposed and traditional model increase with the TOC content (shown in Fig. 2), the accuracy of the two models are both satisfied (shown in Figs. 3–5). The priority of the new rock physics model is that it is convenient to define the TOC indicator to decouple the elastic effect of TOC (shown in Fig. 6), which contributes to parameterizing the reflectivity with the TOC indicator, then jointing the TOC indicator in the inversion objective function.

3. Seismic reflectivity parameterization

Seismic reflectivity parameterization provides essential support for the AVO inversion (Li et al., 2020; Wang et al., 2022; Zong et al., 2021; Zong and Ji, 2020). Combining the equivalent elastic moduli of source rocks and Gray's approximation, a novel linearized approximation of the P-wave reflection coefficient incorporating the equivalent elastic moduli of inorganic rock (K^E and μ^E), density, and TOC indicator (F_{TOC}) is derived.

Gray et al. (1999) represented the P-wave reflection coefficient in terms of bulk modulus (K), shear modulus (μ), and density (ρ) as:

$$R_{pp}(\theta) \approx \left(\frac{1}{4}-\frac{1}{3}\frac{V_S^2}{V_P^2}\right)\sec^2\theta\,\frac{\Delta K}{K}+\frac{V_S^2}{V_P^2}\left(\frac{1}{3}\sec^2\theta-2\sin^2\theta\right)\,\frac{\Delta\mu}{\mu} + \left(\frac{1}{2}-\frac{1}{4}\sec^2\theta\right)\,\frac{\Delta\rho}{\rho}, \tag{26}$$

where θ is incident angle, V_P and V_S represent P-wave and S-wave velocities, respectively. $\frac{\Delta K}{K}$, $\frac{\Delta\mu}{\mu}$ and $\frac{\Delta\rho}{\rho}$ are the reflectivity of the bulk modulus, shear modulus and rock density, respectively.

According to Eq. (24) and Eq. (25), $\frac{\Delta K}{K}$ and $\frac{\Delta\mu}{\mu}$ can be expressed as

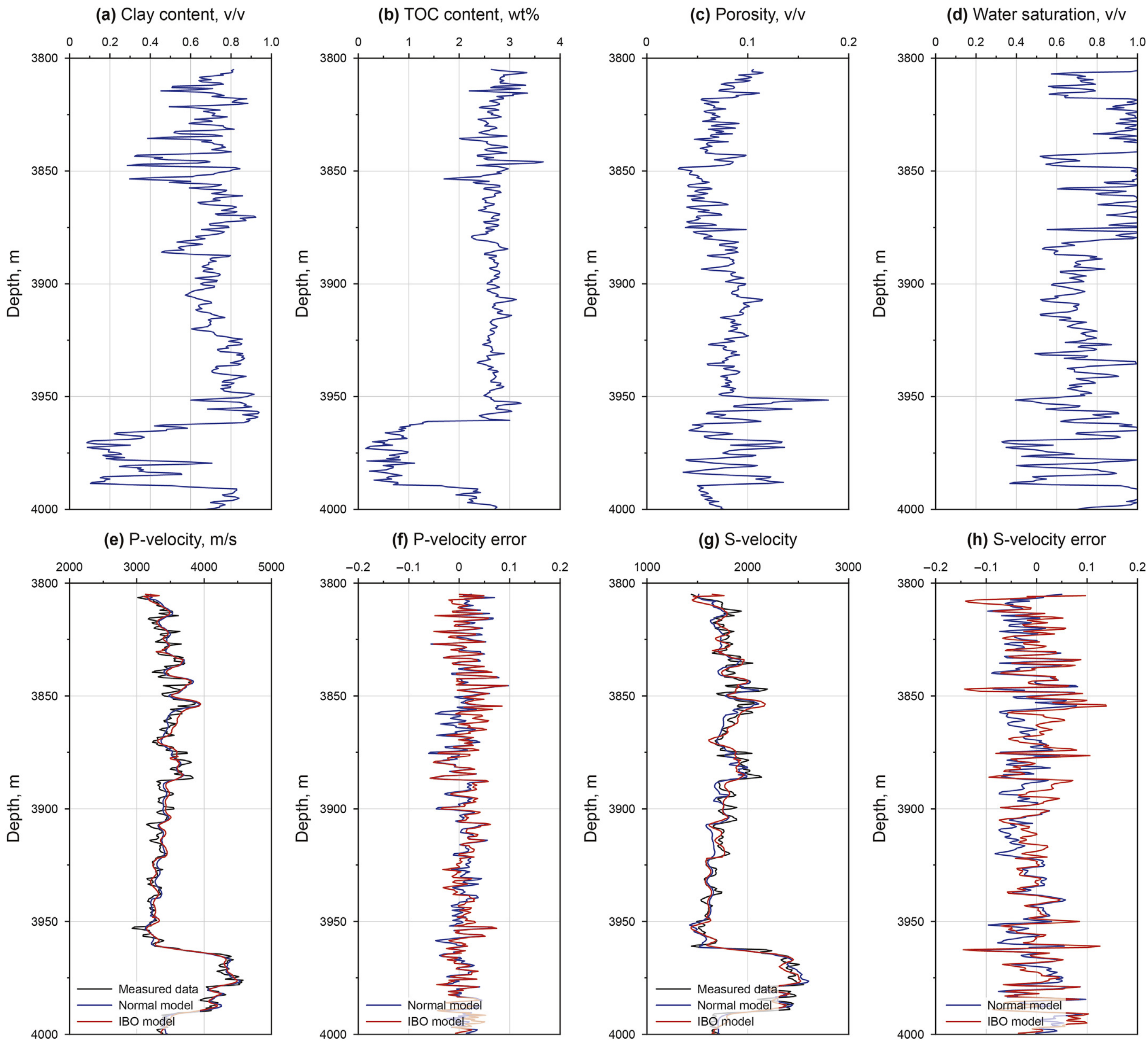

Fig. 3. Interpreted well-loggings and prediction velocities of actual well-A. (a) Clay content, (b) TOC, (c) porosity, (d) water saturation, (e) P-wave velocity, (f) P-wave velocity error, (g) S-wave velocity, (h) S-wave velocity error.

$$\frac{\Delta K}{K}=\frac{\Delta\left(K^{E}F_{TOC}{}^{P_{k}}+K_{k}\right)}{K^{E}F_{TOC}{}^{P_{k}}+K_{k}}=\frac{\Delta K^{E}F_{TOC}{}^{P_{k}}+K^{E}\Delta\left(F_{TOC}{}^{P_{k}}\right)}{K^{E}F_{TOC}{}^{P_{k}}+K_{k}}, \tag{27}$$

$$\frac{\Delta\mu}{\mu}=\frac{\Delta\left(\mu^{E}F_{TOC}{}^{Q_{k}}+\mu_{k}\right)}{\mu^{E}F_{TOC}{}^{Q_{k}}+\mu_{k}}=\frac{\Delta\mu^{E}F_{TOC}{}^{Q_{k}}+\mu^{E}\Delta\left(F_{TOC}{}^{Q_{k}}\right)}{\mu^{E}F_{TOC}{}^{Q_{k}}+\mu_{k}}, \tag{28}$$

To simplify Eq. (27) and Eq. (28), two scale coefficients are set as:

$$C_{K}=\frac{K^{E}F_{TOC}{}^{P_{k}}}{K^{E}F_{TOC}{}^{P_{k}}+K_{k}}, \tag{29}$$

$$C_{\mu}=\frac{\mu^{E}F_{TOC}{}^{Q_{k}}}{\mu^{E}F_{TOC}{}^{Q_{k}}+\mu_{k}}, \tag{30}$$

Substituting Eq. (29) and Eq. (30) into Eq. (27) and Eq. (28), respectively, and yields:

$$\frac{\Delta K}{K}=C_{K}\left(\frac{\Delta K^{E}}{K^{E}}+\frac{\Delta\left(F_{TOC}{}^{P_{k}}\right)}{F_{TOC}{}^{P_{k}}}\right), \tag{31}$$

$$\frac{\Delta\mu}{\mu}=C_{\mu}\left(\frac{\Delta\mu^{E}}{\mu^{E}}+\frac{\Delta\left(F_{TOC}{}^{Q_{k}}\right)}{F_{TOC}{}^{Q_{k}}}\right), \tag{32}$$

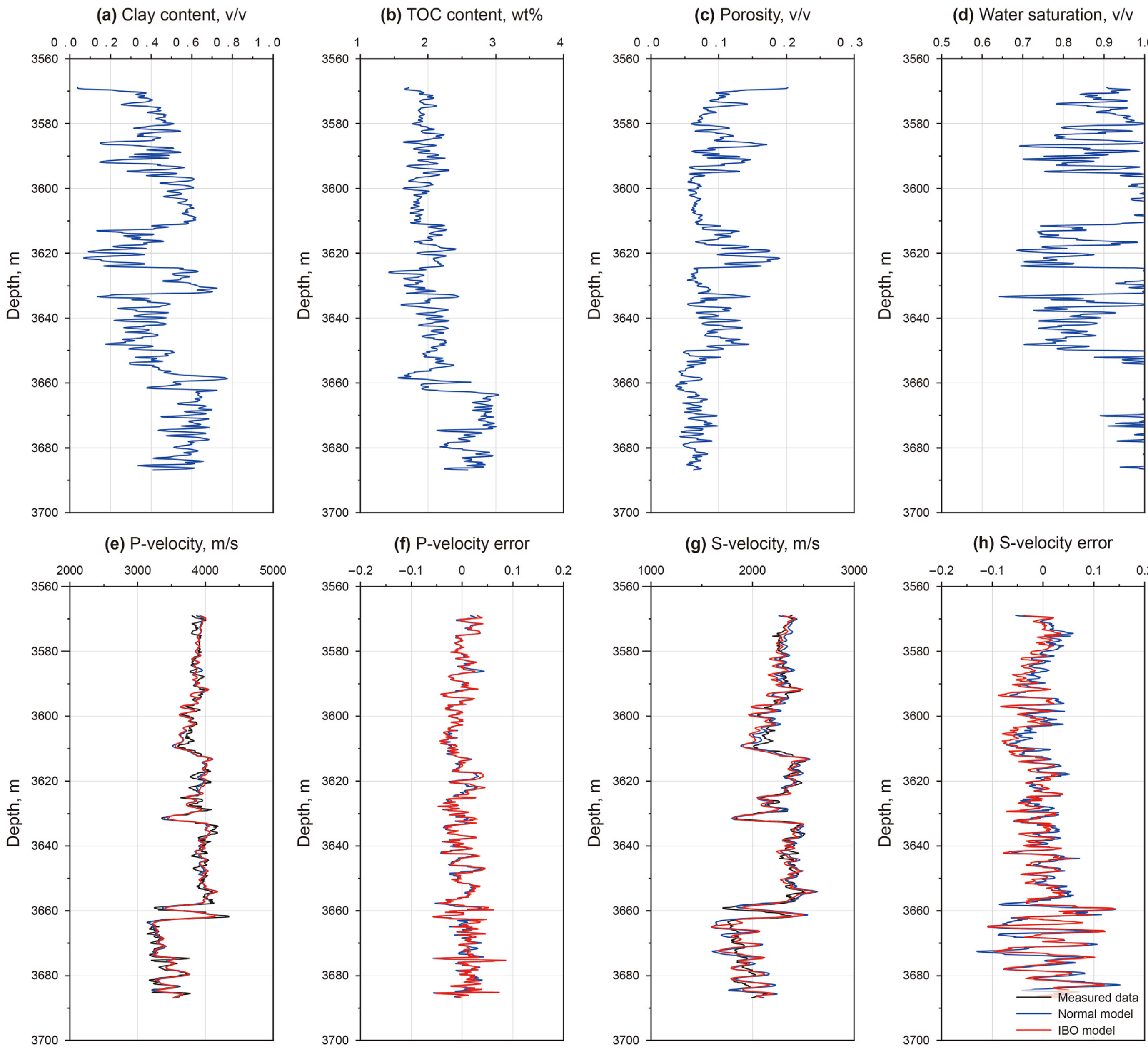

Fig. 4. Interpreted well-loggings and prediction velocities of actual well-B. (a) Clay content, (b) TOC, (c) porosity, (d) water saturation, (e) P-wave velocity, (f) P-wave velocity error, (g) S-wave velocity, (h) S-wave velocity error.

where

$$\frac{\Delta\left({F_{TOC}}^{P_k}\right)}{{F_{TOC}}^{P_k}}=\frac{P_k {F_{TOC}}^{P_k-1}\Delta F_{TOC}}{{F_{TOC}}^{P_k}}=\frac{P_k\Delta F_{TOC}}{F_{TOC}}, \tag{33}$$

$$\frac{\Delta\left({F_{TOC}}^{Q_k}\right)}{{F_{TOC}}^{Q_k}}=\frac{Q_k {F_{TOC}}^{Q_k-1}\Delta F_{TOC}}{{F_{TOC}}^{Q_k}}=\frac{Q_k\Delta F_{TOC}}{F_{TOC}}, \tag{34}$$

then

$$\frac{\Delta K}{K}=C_K\left(\frac{\Delta K^E}{K^E}+\frac{P_k\Delta F_{TOC}}{F_{TOC}}\right), \tag{35}$$

$$\frac{\Delta\mu}{\mu}=C_\mu\left(\frac{\Delta\mu^E}{\mu^E}+\frac{Q_k\Delta F_{TOC}}{F_{TOC}}\right), \tag{36}$$

Substituting Eq. (35) and Eq. (36) into Eq. (26) yields

$$\begin{aligned}R_{PP}(\theta)\approx{}& C_K\left(\frac{1}{4}-\frac{1}{3}\frac{V_S^2}{V_P^2}\right)\sec^2\theta\frac{\Delta K^E}{K^E}+C_\mu\frac{V_S^2}{V_P^2}\left(\frac{1}{3}\sec^2\theta\right.\\&\left.-2\sin^2\theta\right)\frac{\Delta\mu^E}{\mu^E}+\left(\frac{1}{2}-\frac{1}{4}\sec^2\theta\right)\frac{\Delta\rho}{\rho}+\left[\frac{1}{4}C_K P_k\sec^2\theta\right.\\&\left.-2C_\mu Q_k\frac{V_S^2}{V_P^2}\sin^2\theta+\frac{1}{3}\frac{V_S^2}{V_P^2}\sin^2\theta\left(C_\mu Q_k-C_K P_k\right)\right]\frac{\Delta F_{TOC}}{F_{TOC}},\end{aligned} \tag{37}$$

where $\frac{\Delta K^E}{K^E}$ is the inorganic equivalent bulk modulus reflectivity, $\frac{\Delta\mu^E}{\mu^E}$

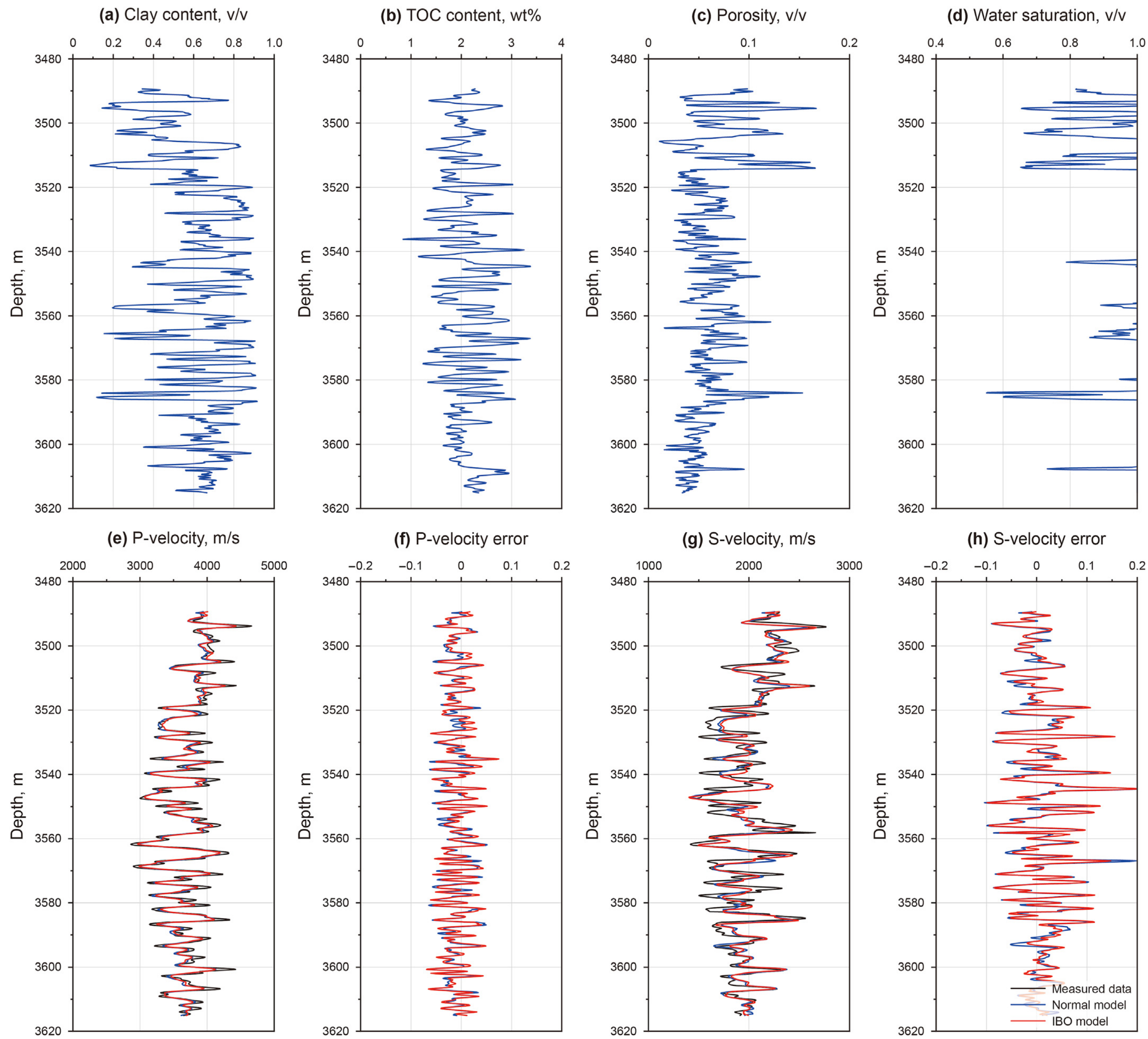

Fig. 5. Interpreted well-loggings and prediction velocities of actual well-C. (a) Clay content, (b) TOC, (c) porosity, (d) water saturation, (e) P-wave velocity, (f) P-wave velocity error, (g) S-wave velocity, (h) S-wave velocity error.

is the inorganic equivalent shear modulus reflectivity, $\frac{\Delta\rho}{\rho}$ is density reflectivity, and $\frac{\Delta F_{TOC}}{F_{TOC}}$ is the reflectivity of TOC indicator, they can be expressed as:

$$\frac{\Delta K^E}{K^E} = \frac{2\left(K_1^E - K_2^E\right)}{\left(K_1^E + K_2^E\right)}, \tag{38}$$

$$\frac{\Delta\mu^E}{\mu^E} = \frac{2\left(\mu_1^E - \mu_2^E\right)}{\left(\mu_1^E + \mu_2^E\right)} \tag{39}$$

$$\frac{\Delta\rho}{\rho} = \frac{2(\rho_1 - \rho_2)}{(\rho_1 + \rho_2)} \tag{40}$$

$$\frac{\Delta F_{TOC}}{F_{TOC}} = \frac{2(F_{TOC1} - F_{TOC2})}{(F_{TOC1} + F_{TOC2})} \tag{41}$$

A three-layer model is constructed from actual data to examine the accuracy of the novel P-wave reflection coefficient approximation in Eq. (37). The TOC, clay content, porosity, and water saturation of each layer are shown in Table 2. The TOC contents of sand and source rock are set to 0.5% and 3.0%, respectively. The model consists of the top negative reflector and the lower positive reflector because the impedance of the middle source rock layer is smaller than those of the upper and lower sand layers.

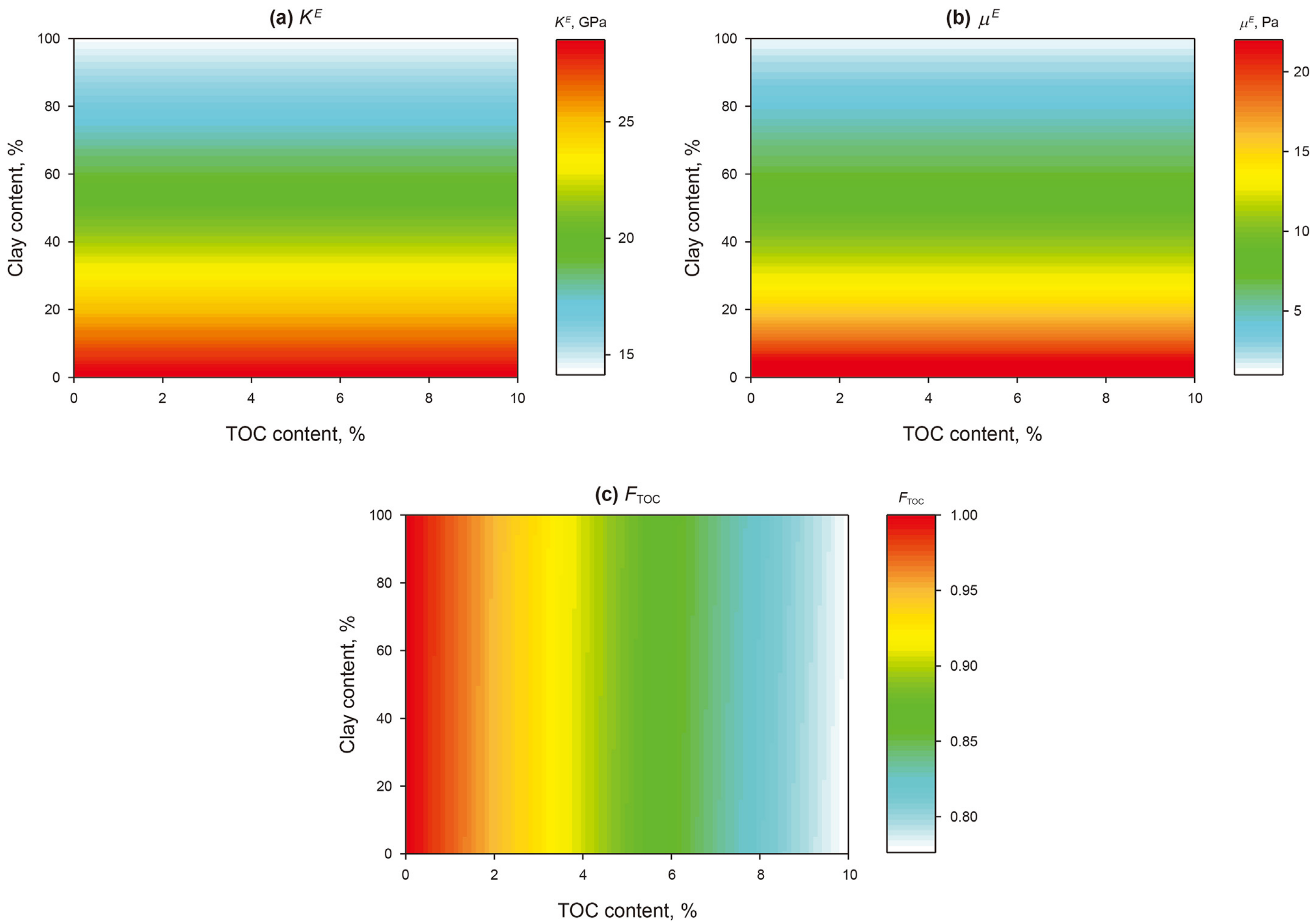

Fig. 6. The sensitivity analysis of elastic parameters and TOC indicator on TOC and clay content. (a) The equivalent bulk modulus of inorganic rock (K^E), (b) the equivalent shear modulus of inorganic rock (μ^E), (c) the TOC indicators (F_{TOC}).

Table 2
The physical properties of the three-layer model.

Layer	TOC, w%	Clay content, v/v	Porosity, v/v	Water saturation, v/v
Top sand	0.5%	10%	20%	100%
Source rock	3.0%	75%	10%	100%
Bottom sand	0.5%	10%	20%	60%

Fig. 7a displays the reflection coefficients of the negative reflector calculated with the exact Zoeppritz equation (Zoeppritz, 1919), Aki-Richards approximation (Aki and Richards, 1980), Gray approximation in Eq. (26), and the novel approximation of the TOC indicator (F_{TOC}) in Eq. (37). Fig. 7b displays the comparison of reflection coefficients at the positive reflector. Fig. 7 suggests that the reflection coefficients of the TOC indicator (F_{TOC}) are close to those calculated with the exact Zoeppritz equation and Aki-Richards approximation, Gray approximation until incident angles reach 40°.

The effects of TOC, clay content, porosity, and water saturation on the AVO reflection coefficients are discussed for the negative reflector, as shown in Fig. 8. From Fig. 8, we conclude that porosity significantly influences the AVO reflection coefficients, followed by TOC and clay content, and water saturation has little effect.

From the perspective of elastic parameters, the effects of the inorganic equivalent bulk modulus (K^E), inorganic equivalent bulk modulus (μ^E), density (ρ) and TOC indicator (F_{TOC}) on the AVO reflection coefficients are displayed in Fig. 9. Fig. 9 illustrates that the K^E, μ^E, ρ and F_{TOC} all contribute to the P-wave reflectivity. K^E and μ^E have the most significant influences, followed by density (ρ), and the influence of F_{TOC} is smaller than that of K^E, μ^E and density (ρ). However, the contributions of K^E, μ^E, ρ and F_{TOC} to the reflection coefficients are highly related, which may lead to the increased difficulty of robustly inverting them from the pre-stack seismic data (Downton, 2005; Gidlow et al., 1993; Zong et al., 2015). Therefore, the decorrelation of those four parameters is needed in the inversion algorithm to enhance the solvability and stability of inverted results (Zong and Yin, 2016; Zong et al., 2015).

4. TOC prediction with AVO inversion

The TOC indicator is estimated by seismic AVO inversion under the Bayesian scheme. Simplifying Eq. (37) as

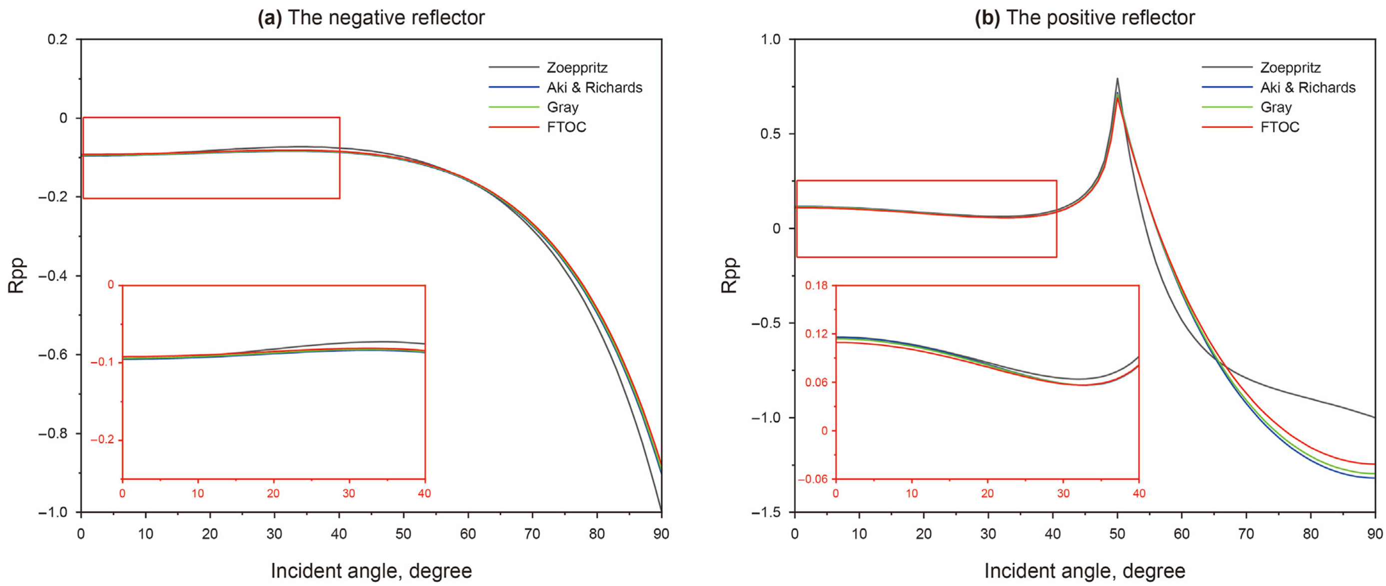

Fig. 7. Comparison of the P-wave reflection coefficients calculated by the exact Zoeppritz equation, Aki-Richards approximation, Gray approximation and Eq. (37) of reflectors. (a) The positive reflector, (b) the negative reflector.

$$R_{pp}(\theta) = A(\theta)R_{KE} + B(\theta)R_{\mu E} + C(\theta)R_{\rho} + D(\theta)R_{FTOC}, \tag{42}$$

where,

$$A(\theta) = C_K\left(\frac{1}{4} - \frac{1}{3}\frac{V_S^2}{V_P^2}\right)\sec^2\theta, \tag{43}$$

$$B(\theta) = C_\mu\frac{V_S^2}{V_P^2}\left(\frac{1}{3}\sec^2\theta - 2\sin^2\theta\right), \tag{44}$$

$$C(\theta) = \left(\frac{1}{2} - \frac{1}{4}\sec^2\theta\right), \tag{45}$$

$$D(\theta) = \frac{1}{4}C_K P_\mathrm{k}\sec^2\theta - 2C_\mu Q_\mathrm{k}\frac{V_S^2}{V_P^2}\sin^2\theta + \frac{1}{3}\frac{V_S^2}{V_P^2}\sin^2\theta(C_\mu Q_\mathrm{k} - C_K P_\mathrm{k}). \tag{46}$$

The prior probability distribution and likelihood function of the model parameters are set to the Cauchy distribution and Gaussian distribution, respectively (Alemie and Sacchi, 2011; Buland and Omre, 2003; Zong and Yin, 2016, 2017). To enhance the stability of simultaneous inversion for four parameters, the smooth initial model constraint is added to inversion objective function (Zong and Yin, 2016, 2017). Furthermore, the preconditioned conjugate gradient method (PCGM) is also used to weaken the strong correlation among the model parameters (Zong and Yin, 2016, 2017).

Maximize the posterior distribution of the model parameters to get the objective function equation:

$$F(\mathbf{R}) = (\mathbf{D} - \mathbf{GR})^T(\mathbf{D} - \mathbf{GR}') + 2\sigma_n^2\sum_{i=1}^{K}\ln\left(1 + \mathbf{R}_i^2\big/\sigma_\mathrm{k}^2\right) + \Lambda, \tag{47}$$

where $\mathbf{R}$ is the reflectivity matrix of model parameters and is set as

$$\mathbf{R} = [\,\mathbf{R}_{KE} \quad \mathbf{R}_{\mu E} \quad \mathbf{R}_{\rho} \quad \mathbf{R}_{FTOC}\,] = \left[\frac{\Delta K^E}{K^E} \quad \frac{\Delta\mu^E}{\mu^E} \quad \frac{\Delta\rho}{\rho} \quad \frac{\Delta F_{TOC}}{F_{TOC}}\right]. \tag{48}$$

In Eq. (47), $\mathbf{G}$ is the wavelet matrix incorporating the weighting coefficients in Eq. (42), σ_n^2 is the noise variance, σ_k^2 is the variance of parameters to be estimated, $\mathbf{D}$ is the observed seismic data, and

$$\Lambda = \lambda_1(\boldsymbol{\eta}_1 - \mathbf{P}_1\mathbf{R}_1)^T(\boldsymbol{\eta}_1 - \mathbf{P}_1\mathbf{R}_1) + \lambda_2(\boldsymbol{\eta}_2 - \mathbf{P}_2\mathbf{R}_2)^T(\boldsymbol{\eta}_2 - \mathbf{P}_2\mathbf{R}_2) + \lambda_1(\boldsymbol{\eta}_3 - \mathbf{P}_3\mathbf{R}_3)^T(\boldsymbol{\eta}_3 - \mathbf{P}_3\mathbf{R}_3) + \lambda_4(\boldsymbol{\eta}_4 - \mathbf{P}_4\mathbf{R}_4)^T(\boldsymbol{\eta}_4 - \mathbf{P}_4\mathbf{R}_4), \tag{49}$$

where, λ_i is the constraint coefficient for the i th model parameter (including K^E, μ^E, ρ, and F_{TOC}). The λ_i selection is decided by the seismic data quality because λ_i is the constraint parameter of the smooth initial model. If the signal-to-noise ratio of seismic data is high, the small value of λ_i is set in this situation. Conversely, it leads to a higher λ_i when the signal-to-noise ratio of seismic data is small, which means that the inversion results will depend more on the initial smooth model.

$$P_i = \int_{t_0}^{t_i} \mathrm{d}\tau, \tag{50}$$

$$\boldsymbol{\eta}_i = 1\,/\,2{*}\ln(\mathbf{m}_i\,/\,m_{i0}), \tag{51}$$

$$\mathbf{m} = [\,\mathbf{m}_1 \quad \mathbf{m}_2 \quad \mathbf{m}_3 \quad \mathbf{m}_4\,] = [\,K^E \quad \mu^E \quad \rho \quad FTOC\,], \tag{52}$$

and m_{i0} is the initial value of the i th model parameter (Zong and Yin, 2016, 2017; Zong et al., 2015).

Due to the small nonlinearity of Eq. (47), IRLS strategy is utilized to optimize and solve the objective function in Eq. (47) (Daubechies et al., 2010; Zong et al., 2021).

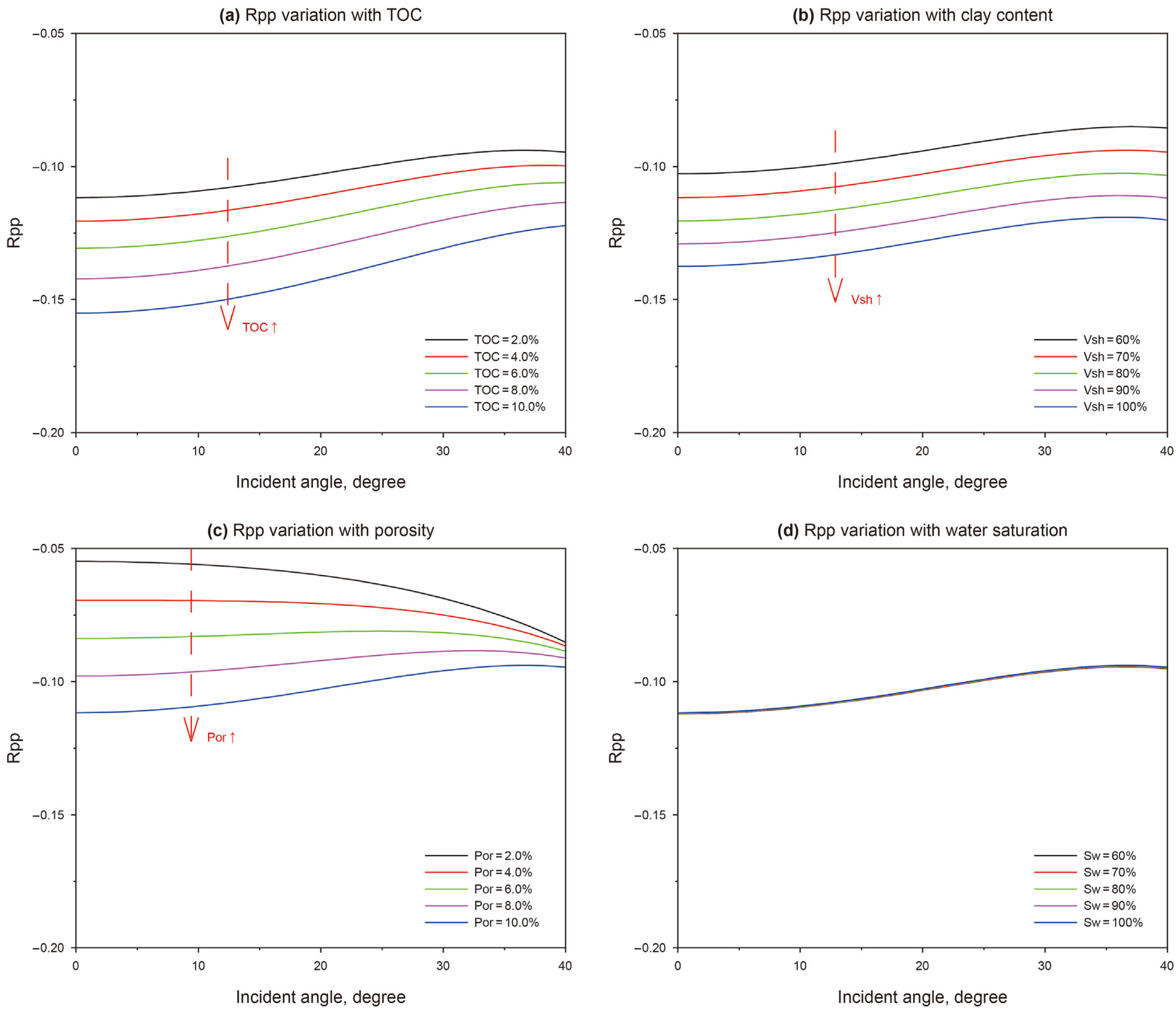

Fig. 8. The effects of TOC, clay content, porosity and water saturation on the proposed P-wave reflectivity. (a) TOC content, (b) clay content, (c) porosity, (d) water saturation.

4.1. 1D model test

The data of actual well-A and well-B are used to test the feasibility of the proposed AVO inversion method. The proposed rock physics model estimates the original curves of model parameters (including K^E, μ^E, ρ, and F_{TOC}). The initial models are obtained by smoothing the original curves 60 times. The synthetic data used for the 1D model test is based on the new approximation of P-wave reflectivity derived in the paper. Adding a Gaussian random noise with differential signal-to-noise ratios (S/N) to the actual synthetic seismic data can further test the stability of the inversion results, as displayed in Fig. 10. Figs. 11–14 are the corresponding estimated results of well-A using the proposed AVO inversion method. From Figs. 11–14, we can get excellent estimation results of K^E, μ^E, and F_{TOC} from synthetic seismic with different noise levels. However, the inversion results of the density term are inferior to those of other parameters under noise testing. Two reasons lead to the unsatisfactory inversion results of density. One is that the absolute contributions of the density are smaller than other parameters, and the other is that the density's and other parameters' contributions are highly related. The unstable density inversion is a common problem in pre-stack seismic inversion, as illustrated by Zong et al. (2015) and Zong and Sun (2022).

The actual well-B is also used to test the proposed AVO inversion method. Fig. 15 shows the synthetic angle gathers of well-B with different noise levels. Figs. 16–19 are the comparisons of the original model logs (blue lines) and inversion result logs (red lines) using the synthetic traces with different noise levels. The inversion results of well-B are the same as those of well-A, maintaining the satisfactory inversion results of K^E, μ^E, and F_{TOC}, and reappearing the inferior effect of density. Due to the anomaly of the density loggings at 2.60 s–2.67 s, the inversion results of density

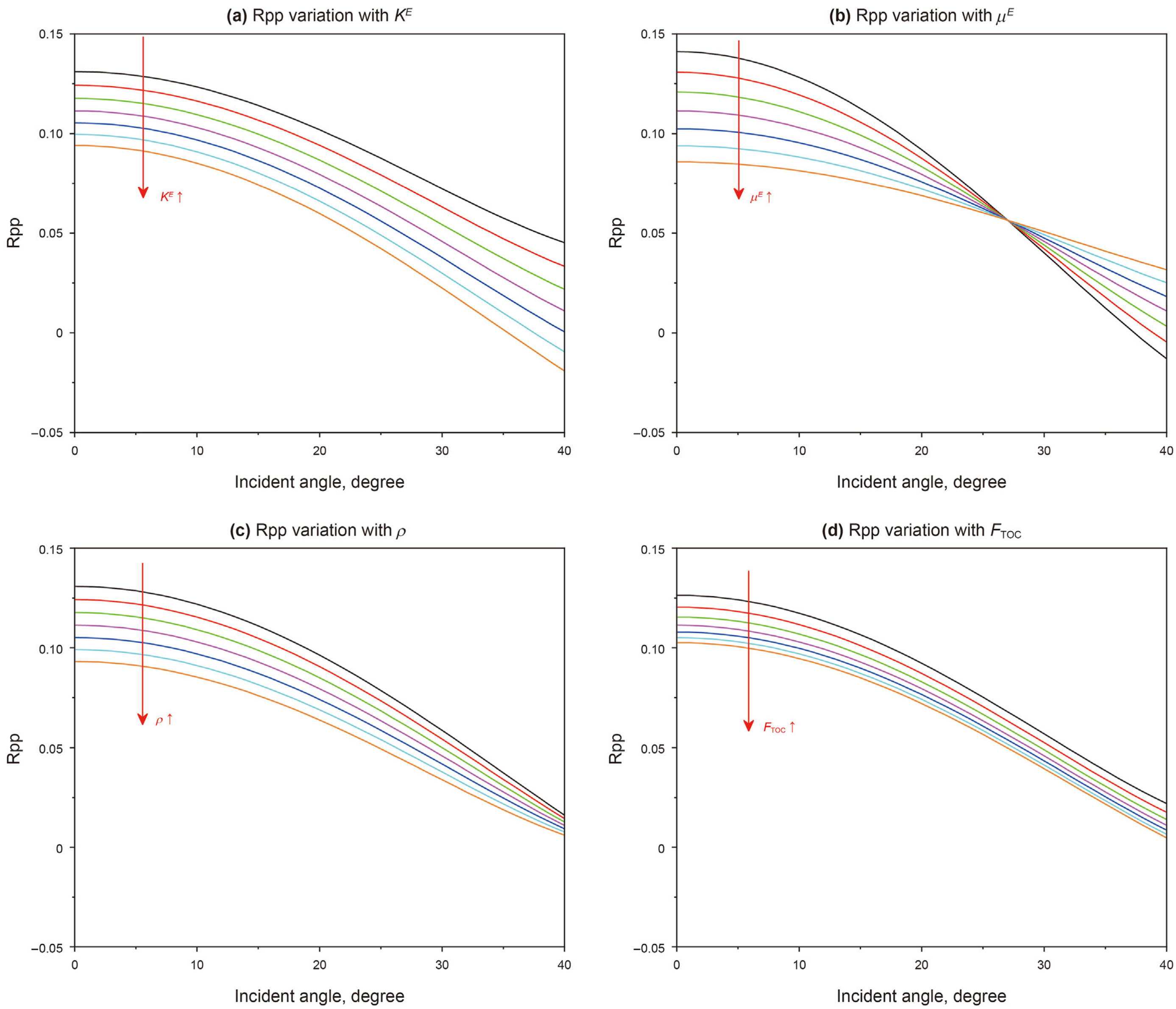

Fig. 9. The effects of equivalent bulk modulus of inorganic rock(K^E), equivalent shear modulus of inorganic rock (μ^E), density (ρ) and TOC indicator(F_{TOC}) on the proposed P-wave reflectivity. (a) K^E, (b) μ^E, (c) ρ, (d) F_{TOC}.

apparently deviate the original model logs (seen in Fig. 16c). In addition, because the loggings of well-B are more variable than those of well-A, the synthetic angle gathers of well-B are more obvious and more distinguishable (seen in Figs. 10 and 15). Therefore, the inversion results of well B exist little difference and are more stable than those of well-A.

4.2. Field application

We apply the proposed AVO inversion method to predict the TOC of the source rock in southern China. The source rock studied was deposited in lacustrine environment, with TOC values ranging from 0.5 to 4.0 wt% and kerogen is in the low maturity stage. The partial angle stacking seismic profiles of $0^\circ - 8^\circ$, $8^\circ - 16^\circ$, $16^\circ - 24^\circ$, and $24^\circ - 32^\circ$ are displayed in Fig. 20. The black curves in Fig. 20 represent the positions of well-A. The data of actual well-A is utilized to establish initial models for the four inversion parameters and verify the accuracy of the inversion results. The initial models of four parameters are contained by combining the low-frequency components of well-A and geological constraint. The prediction targets are two organic-rich source rocks with TOC mainly more than 1.0%.

Fig. 21 displays the inverted results of K^E, μ^E, ρ, and F_{TOC} by the proposed AVO inversion method. Fig. 21d shows that the inverted result of the TOC indicator (F_{TOC}) agrees well with the original model of well-A. Besides, the anomalously low values of the inverted TOC indicator (F_{TOC}) map the distributions of the source rock layers, where the red arrows represent the responses of source rocks.

Based on the relation between the TOC indicator (F_{TOC}) and TOC, we can directly estimate the TOC profile using the inversion results of the TOC indicator. Fig. 22 shows that the predicted TOC definitely

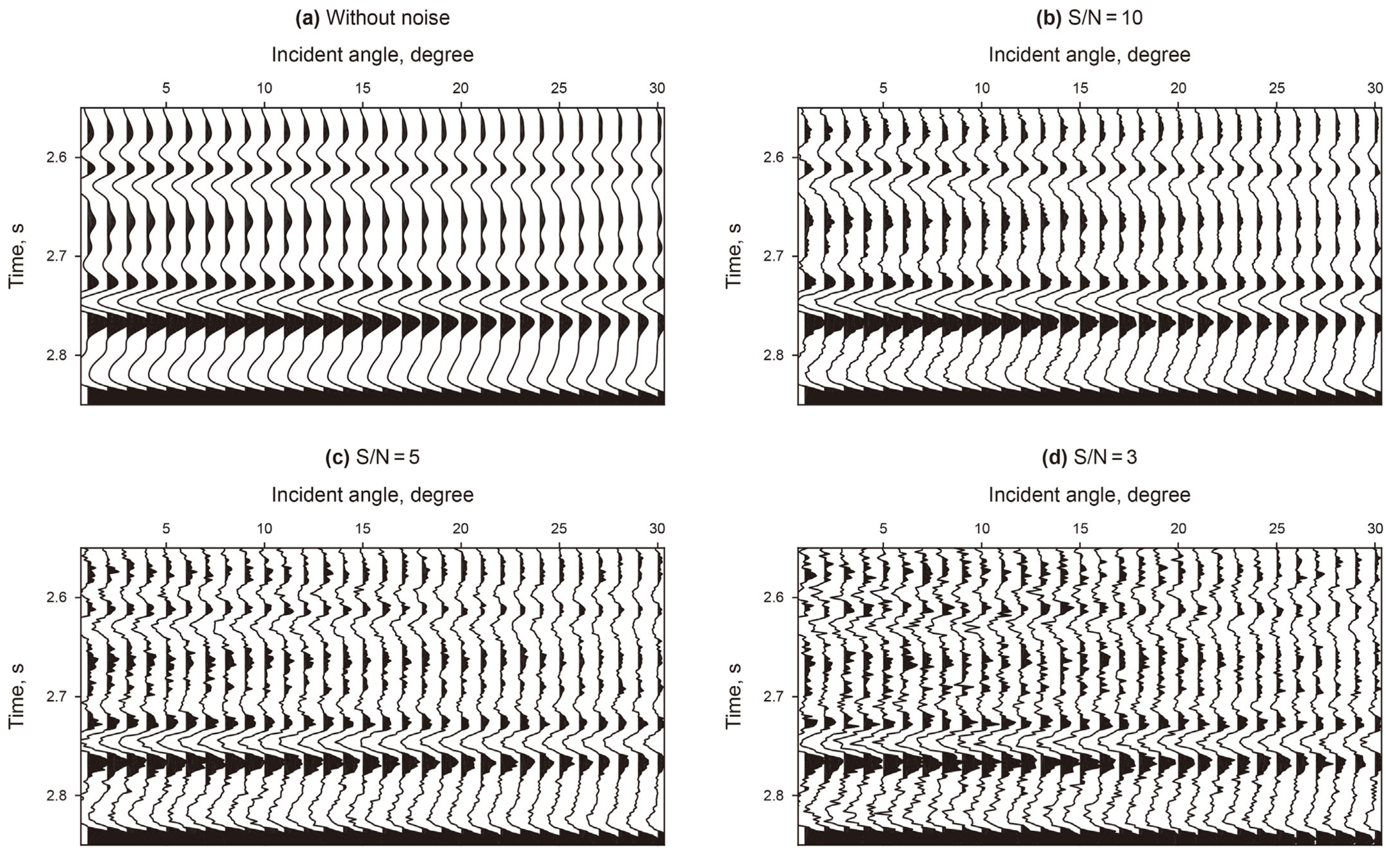

Fig. 10. Synthetic angle gathers of well-A with different noise levels, where (a) shows the case of without noise, (b) shows the case of S/N = 10, (c) shows the case of S/N = 5, and (d) shows the case of S/N = 3.

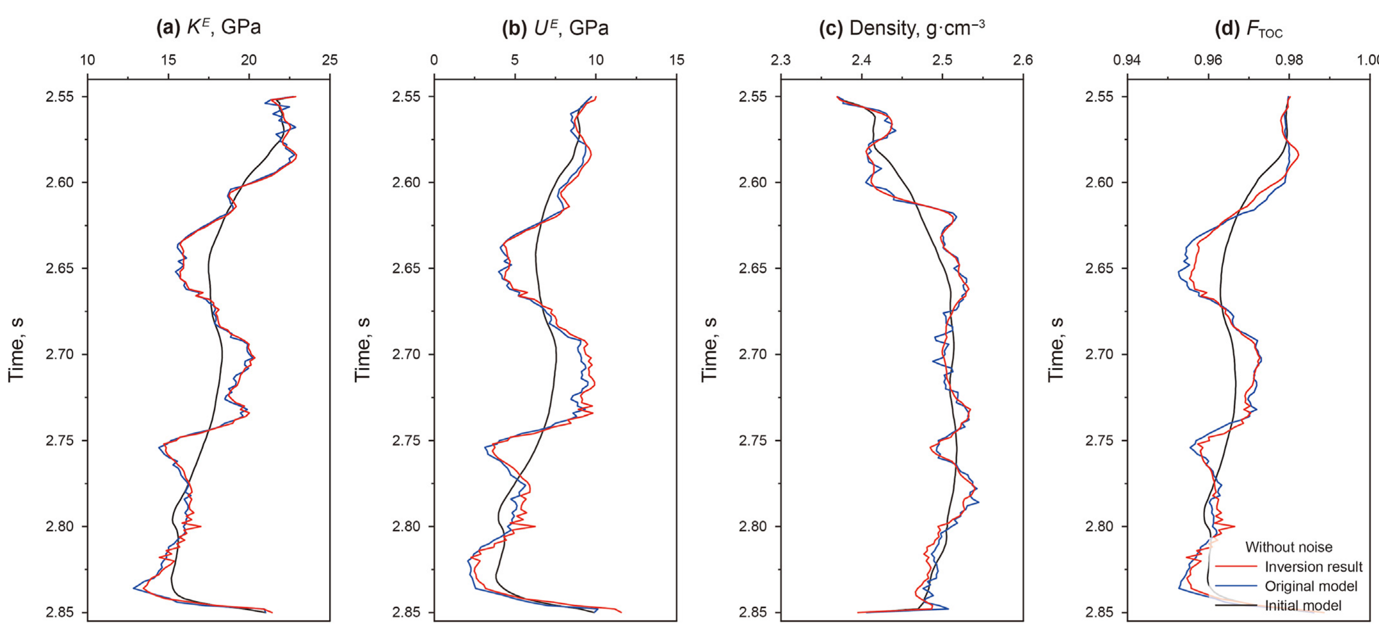

Fig. 11. Comparison of original model logs (blue lines) and inversion result logs (red lines) using the original synthetic traces of well-A, where (a) shows the equivalent bulk modulus of inorganic rock (K^E), (b) shows the equivalent shear modulus of inorganic rock (μ^E), (c) shows the density (ρ), and (d) shows the TOC indicator (F_{TOC}).

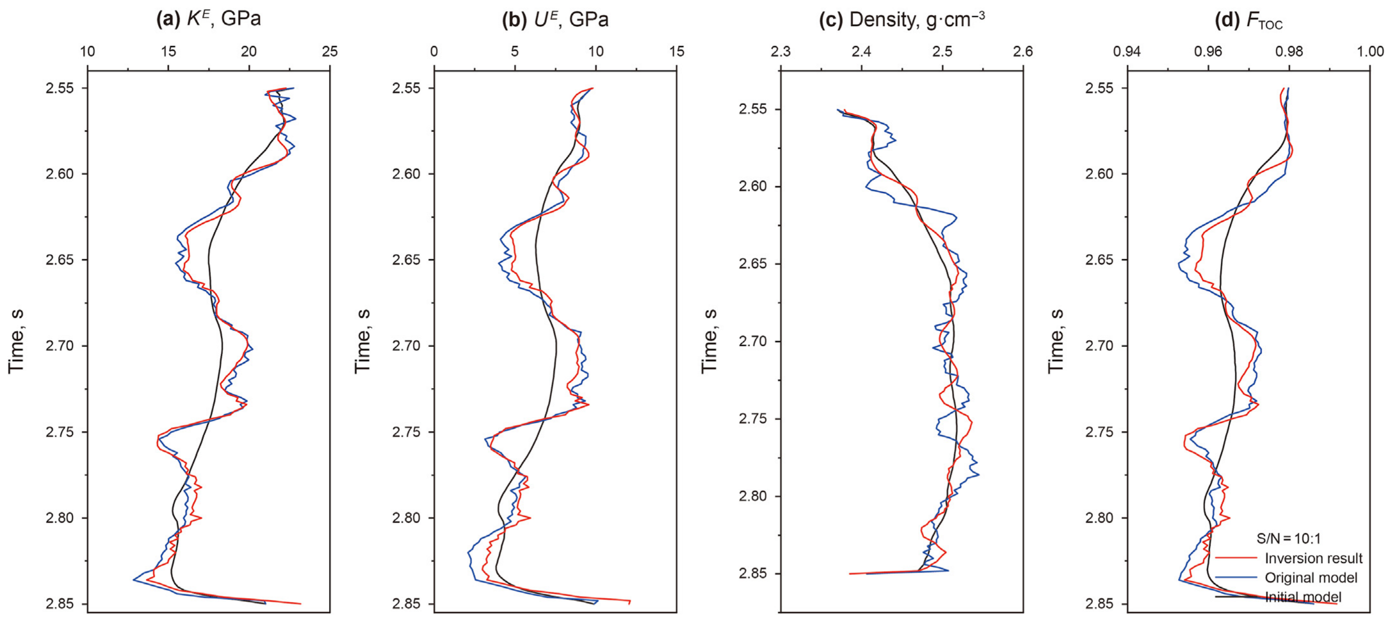

Fig. 12. Comparison of original model logs (blue lines) and inversion result logs (red lines) using the synthetic traces of well-A with S/N = 10, where (a) shows the equivalent bulk modulus of inorganic rock (K^E), (b) shows the equivalent shear modulus of inorganic rock (μ^E), (c) shows the density (ρ), and (d) shows the TOC indicator (F_{TOC}).

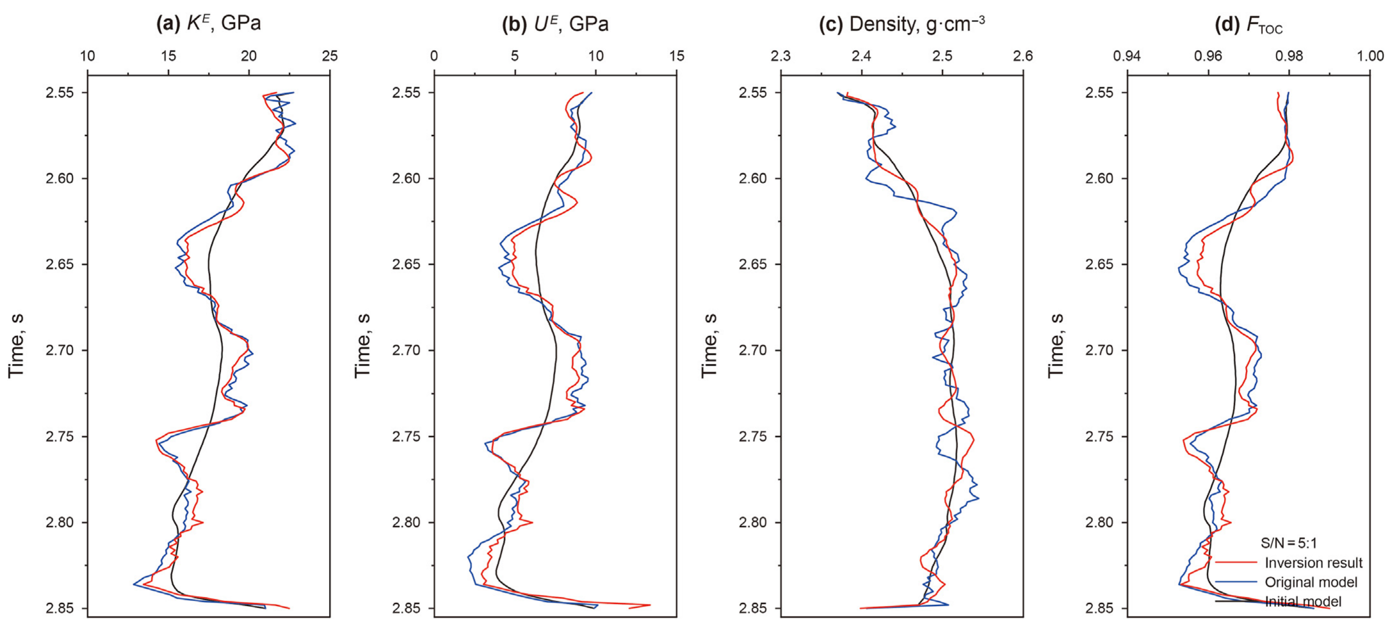

Fig. 13. Comparison of original model logs (blue lines) and inversion result logs (red lines) using the synthetic traces of well-A with S/N = 5, where (a) shows the equivalent bulk modulus of inorganic rock (K^E), (b) shows the equivalent shear modulus of inorganic rock (μ^E), (c) shows the density (ρ), and (d) shows the TOC indicator (F_{TOC}).

and clearly determines the distributions of two source rocks. To compare the superiority and accuracy of the proposed method, we apply the common method published by Amato del Monte et al. (2018), Broadhead et al. (2016), Løseth et al. (2011), and Sahoo et al. (2021) to the same pre-stack seismic data. Amato del Monte et al. (2018), Broadhead et al. (2016), Løseth et al. (2011), and Sahoo et al. (2021) all used the P-wave impedance to predict TOC, which includes two main steps: P-wave impedance inversion and TOC estimation from the inverted P-wave impedance. Fig. 23 shows the correlation fitting the P-wave impedance and estimated TOC logs from wells A, B and C, in which the exponential fitting relation is better than the linearized fitting relation. Fig. 24 shows the inversion results of the traditional prediction method on the same actual seismic profile, where (a) shows the P-wave impedance and (b) shows the converted TOC result. As shown in Fig. 25, we calibrate the TOC predicted by different methods with the calculated TOC of well-A. The goodness of fit of TOC prediction results estimated by the proposed and the traditional method is 66.4% and 34.62%, respectively. The reliability of the TOC predicted by the proposed method is twice that of the traditional method. As shown in Fig. 25, the inversion results of the top and bottom target layers are in good agreement with the TOC calculated logs. However, there

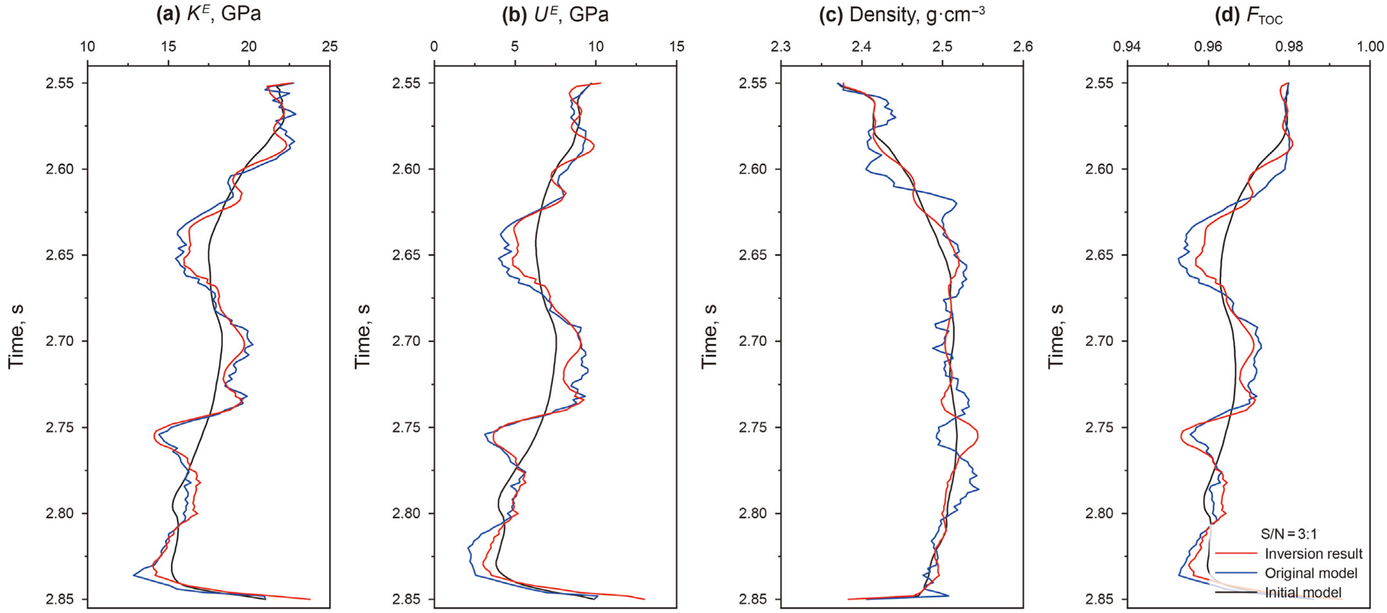

Fig. 14. Comparison of original model logs (blue lines) and inversion result logs (red lines) using the synthetic traces of well-A with S/N = 3, where (a) shows the equivalent bulk modulus of inorganic rock (K^E), (b) shows the equivalent shear modulus of inorganic rock (μ^E), (c) shows the density (ρ), and (d) shows the TOC indicator (F_{TOC}).

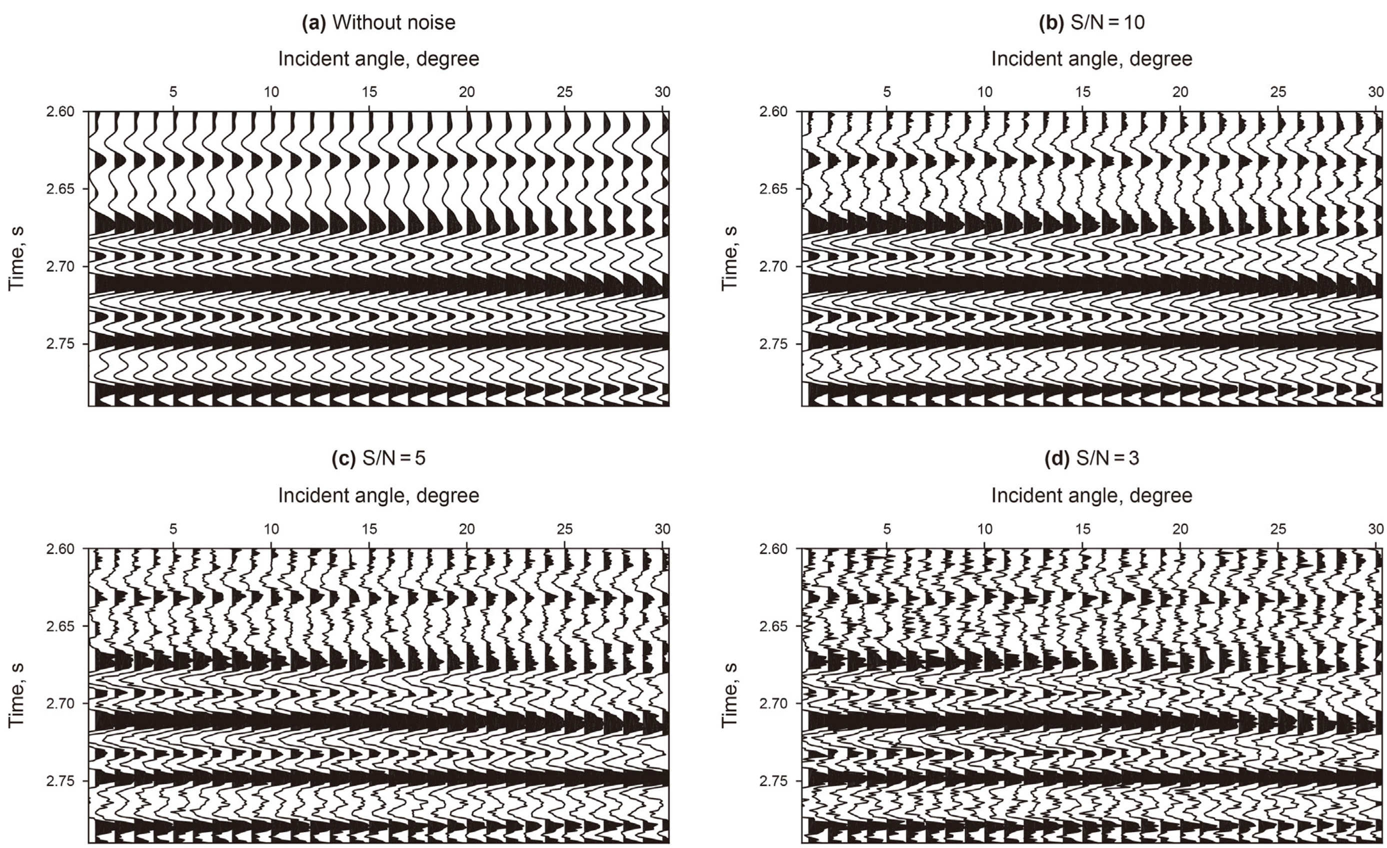

Fig. 15. Synthetic angle gathers of well-B with different noise levels, where (a) shows the case without noise, (b) shows the case of S/N = 10, (c) shows the case of S/N = 5, and (d) shows the case of S/N = 3.

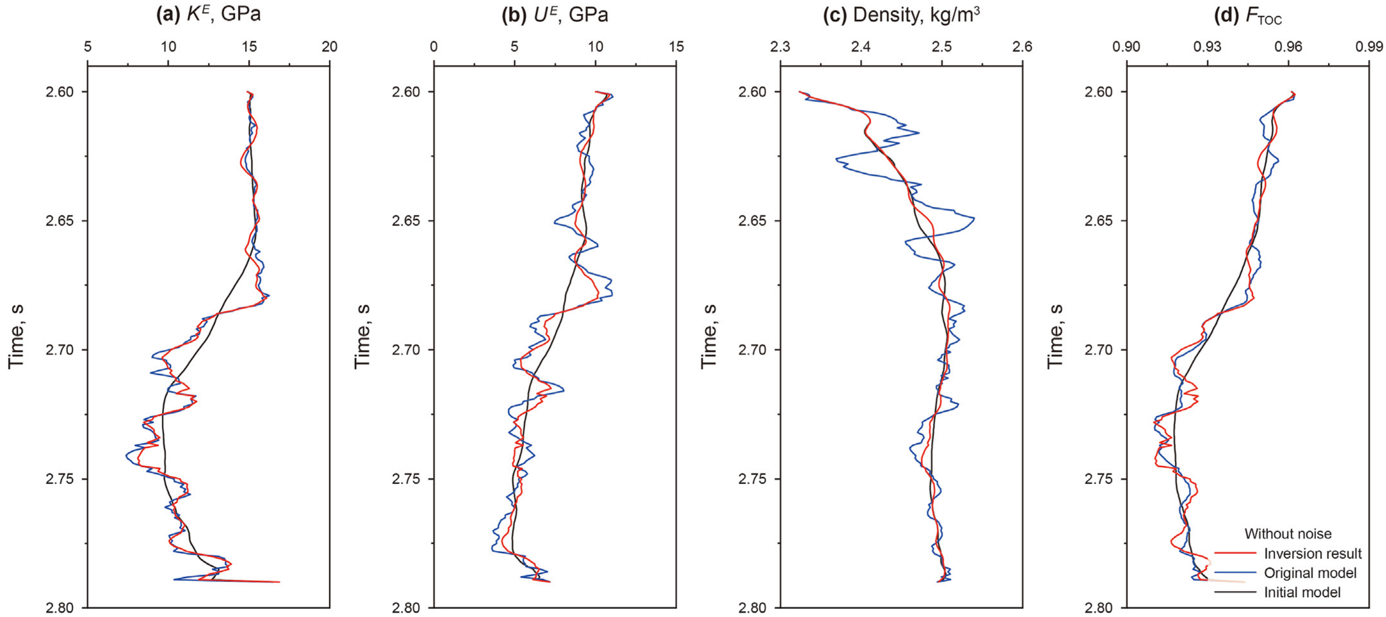

Fig. 16. Comparison of original model logs (blue lines) and inversion result logs (red lines) using the original synthetic traces of well-B, where (a) shows the equivalent bulk modulus of inorganic rock (K^E), (b) shows the equivalent shear modulus of inorganic rock (μ^E), (c) shows the density (ρ), and (d) shows the TOC indicator (F_{TOC}).

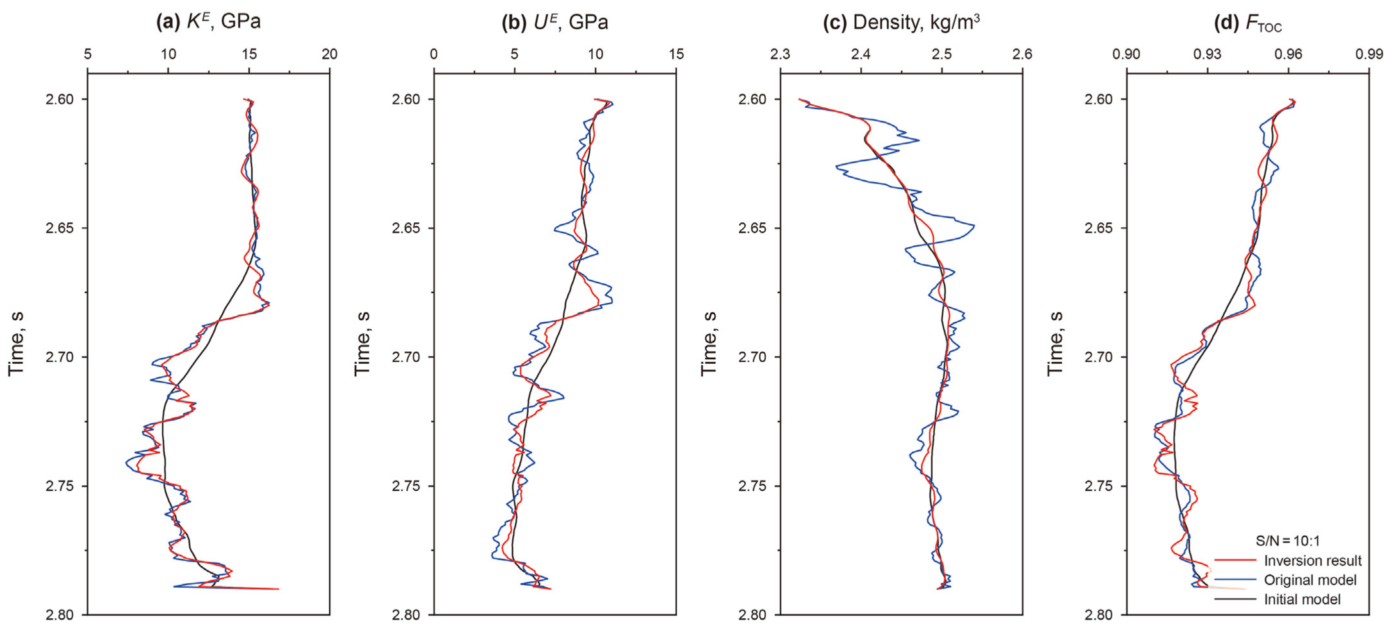

Fig. 17. Comparison of original model logs (blue lines) and inversion result logs (red lines) using the synthetic traces of well-B with S/N = 10, where (a) shows the equivalent bulk modulus of inorganic rock (K^E), (b) shows the equivalent shear modulus of inorganic rock (μ^E), (c) shows the density (ρ), and (d) shows the TOC indicator (F_{TOC}).

are apparent differences between the inversion curves and the calculation TOC logs at 3700–3800 m. Since the interval of 3700–3800 m is not the concerned goal, it lacks experimental information, which probabilistically leads to errors in TOC calculation results, thereby increasing the errors of the inversion results. Given the excellent match between the predicted TOC and calculated TOC, we point out that the TOC can be reliably predicted from the TOC indicator, thereby clearly identifying the distributions of source rocks.

5. Conclusions

To avoid the error of other elastic parameters converting to TOC, we derive and define a TOC indicator to predict TOC directly. We propose a rock physics model to make the equivalent elastic moduli of source rocks parameterized by the equivalent elastic moduli of inorganic rocks and the TOC indicator. Model examples and well-logging tests verify that the proposed rock physics model can be used to accurately delineate the elastic characteristics of source

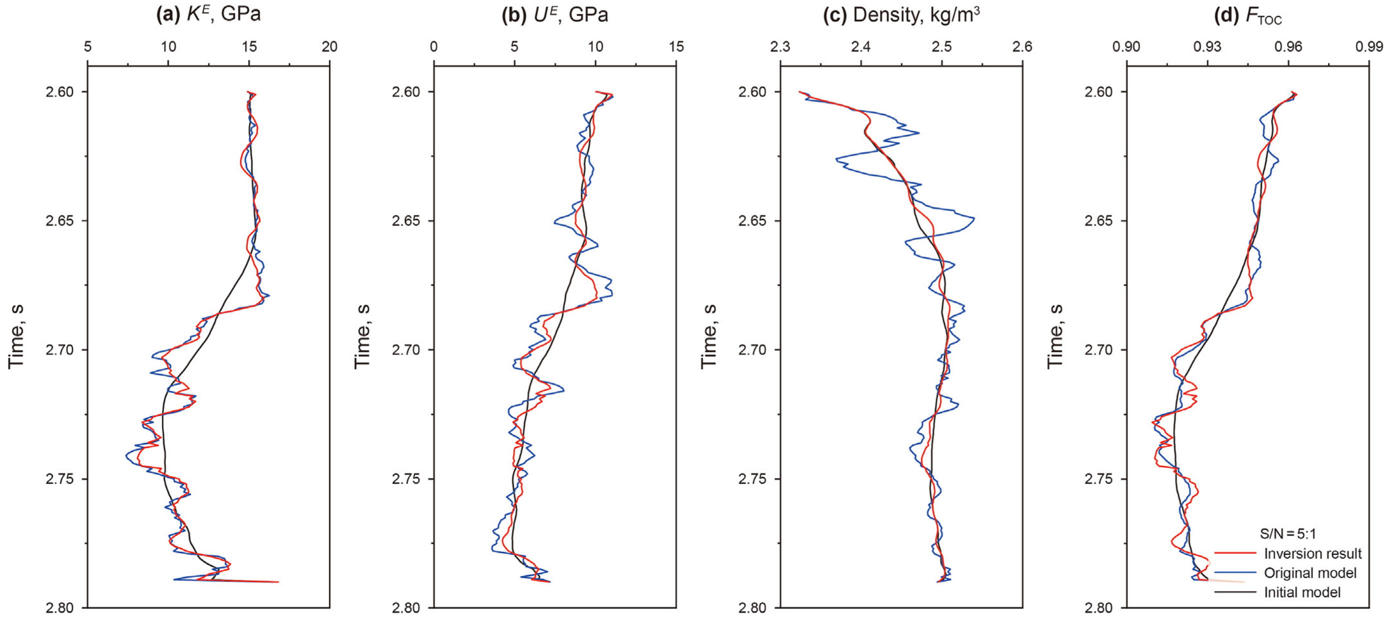

Fig. 18. Comparison of original model logs (blue lines) and inversion result logs (red lines) using the synthetic traces of well-B with S/N = 5, where (a) shows the equivalent bulk modulus of inorganic rock (K^E), (b) shows the equivalent shear modulus of inorganic rock (μ^E), (c) shows the density (ρ), and (d) shows the TOC indicator (F_{TOC}).

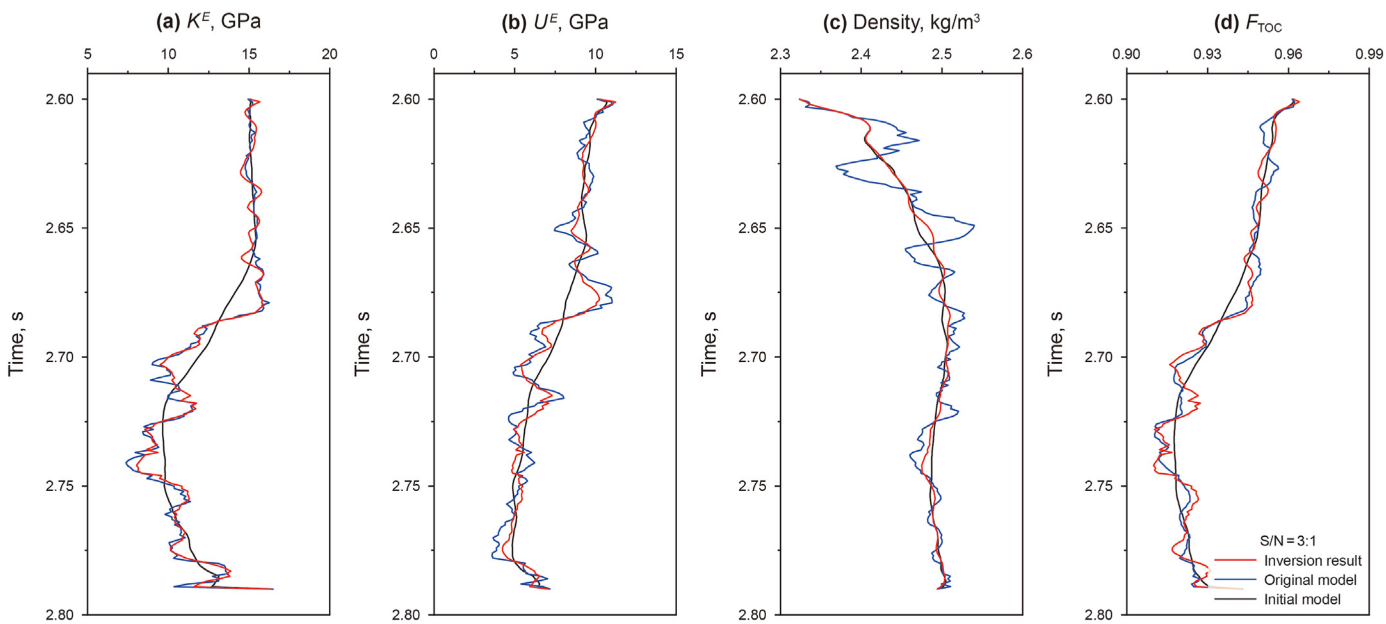

Fig. 19. Comparison of original model logs (blue lines) and inversion result logs (red lines) using the synthetic traces of well-B with S/N = 3, where (a) shows the equivalent bulk modulus of inorganic rock (K^E), (b) shows the equivalent shear modulus of inorganic rock (μ^E), (c) shows the density (ρ), and (d) shows the TOC indicator (F_{TOC}).

rocks and provide a reliable theoretical basis for subsequent applications. To bridge the TOC with seismic data, we further derive a novel linearized approximation of the P-wave reflection coefficient by combining Gray's approximation and the equivalent elastic moduli of source rocks incorporating the TOC indicators. Model simulating results illustrate that the novel linearized approximation agrees well with the exact Zoeppritz equation and the contributions of model parameters meet the requirement of seismic inversion. An AVO inversion method based on the Bayesian theory is proposed to invert the TOC indicator by convoluting the novel P-wave reflection approximation with seismic wavelets as the forward solver. The proposed AVO inversion method has a good application in the field example. Using the inversion results of the TOC indicator, TOC can be directly and reliably predicted. The TOC predicted by the TOC indicator inversion has a more straightforward rock physics interpretation, unlike elastic parameter inversion driven by well logs and experiment data. The AVO inversion method based on Bayesian theory obtains stable and reliable inversion results and has a good application effect in practical applications. The proposed method requires the research source rocks

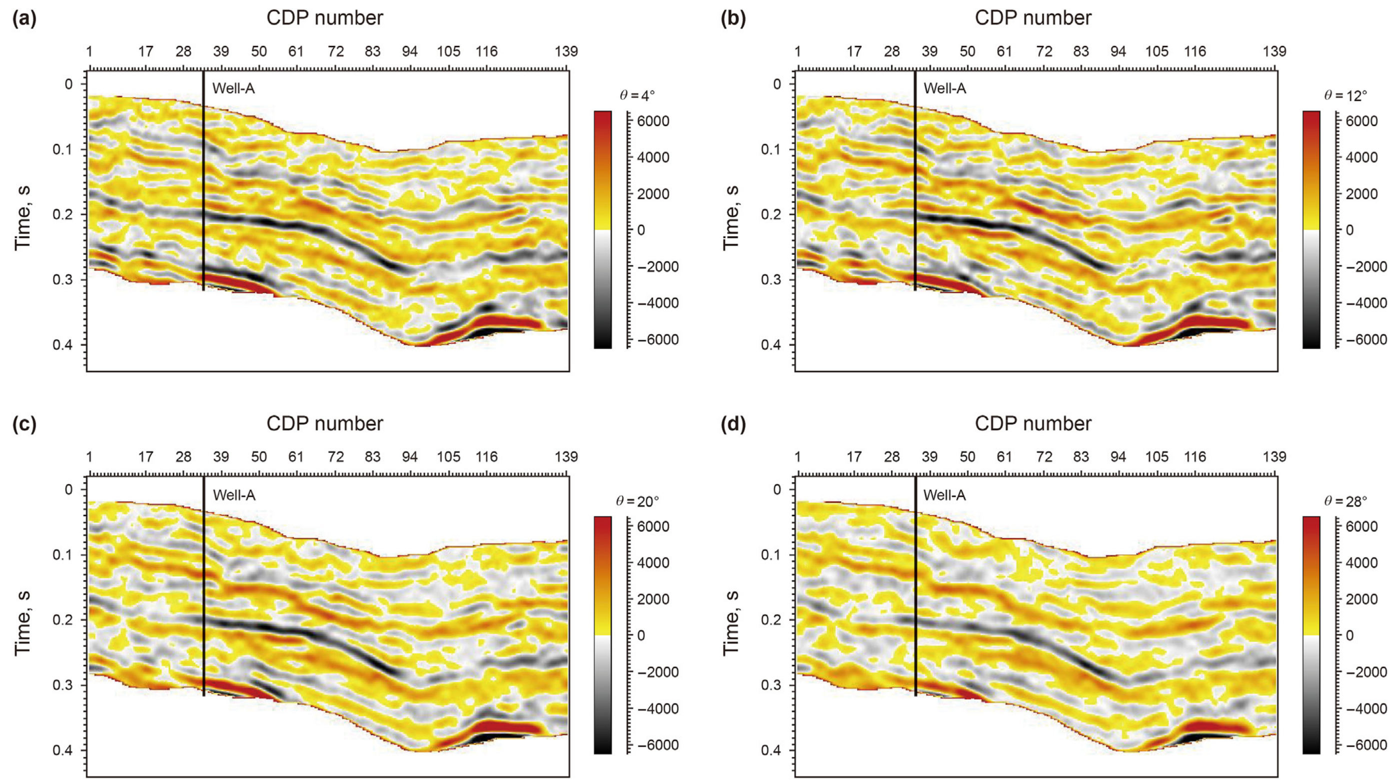

Fig. 20. Partial angle stacking seismic profiles across well-A. (a) Stacking angles of 0°–8°, (b) stacking angles of 8°–16°, (c) stacking angles of 16°–24°, (d) stacking angles of 24°–32°.

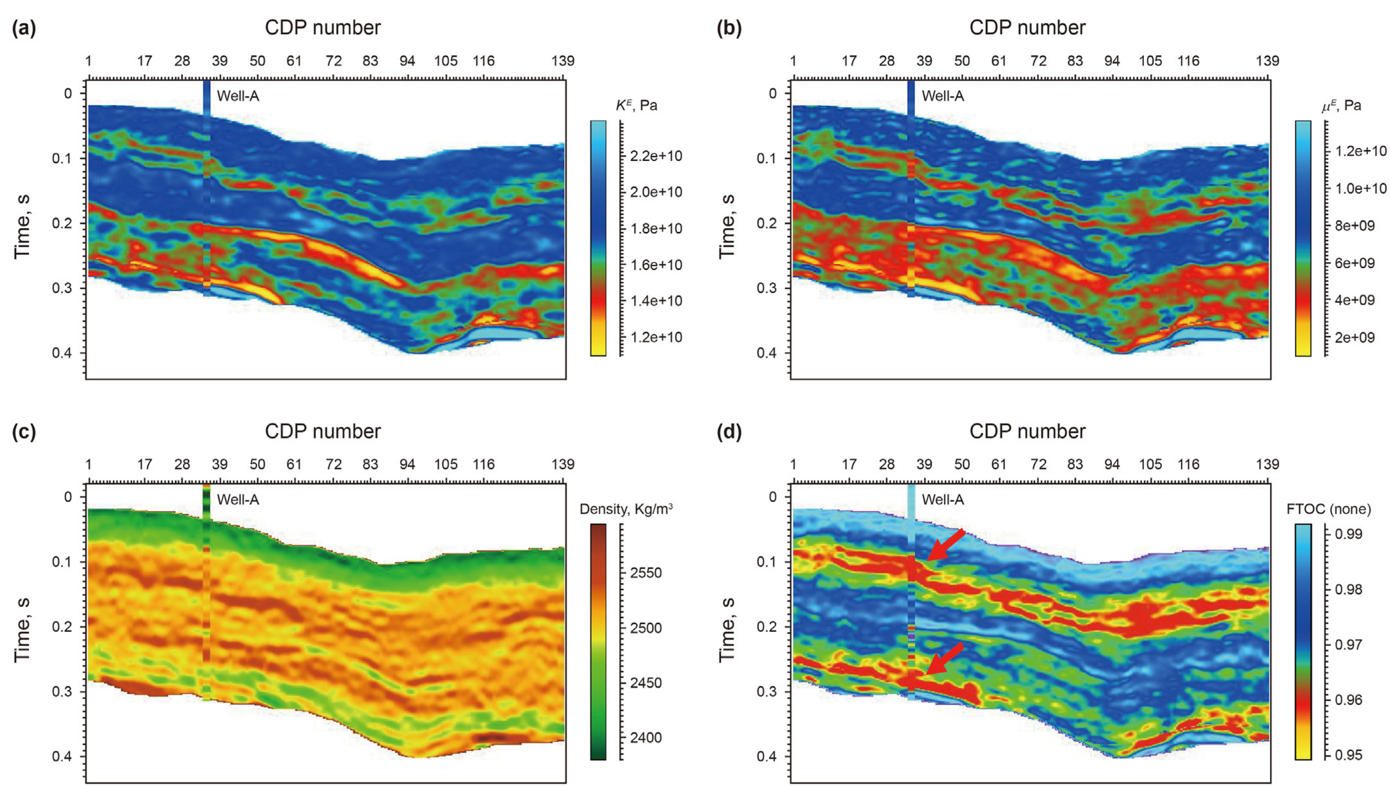

Fig. 21. Inversion results on actual seismic profile. (a) The equivalent bulk modulus of inorganic rock (K^E), (b) the equivalent shear modulus of inorganic rock (μ^E), (c) density (ρ), (d) the TOC indicator (F_{TOC}). The corresponding profiles of well-A are plotted for calibration.

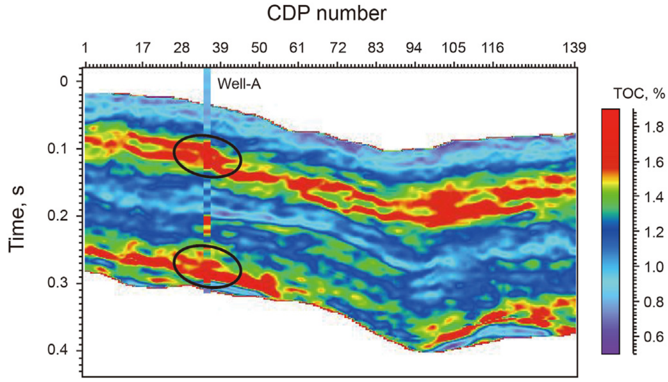

Fig. 22. The TOC prediction results on actual seismic profile. The corresponding TOC profile of well-A is plotted for calibration.

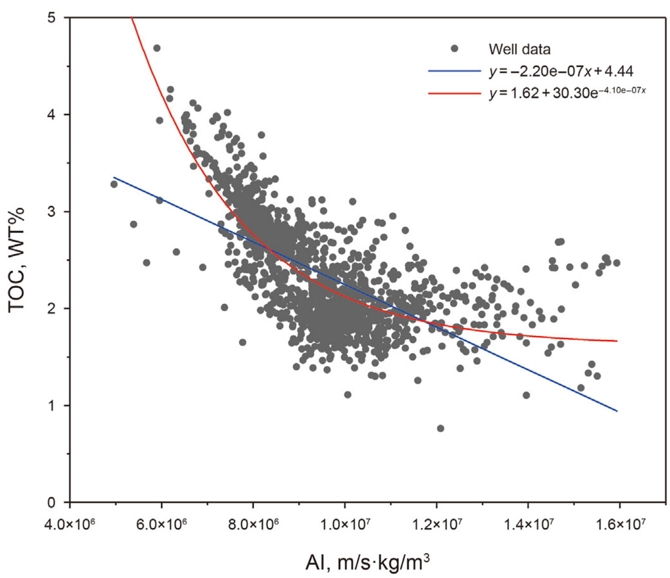

Fig. 23. The correlation fitting the P-wave impedance and estimated TOC logs from wells A, B and C, where the fitting exponential relation is in red, and the fitting linearized relation is in blue.

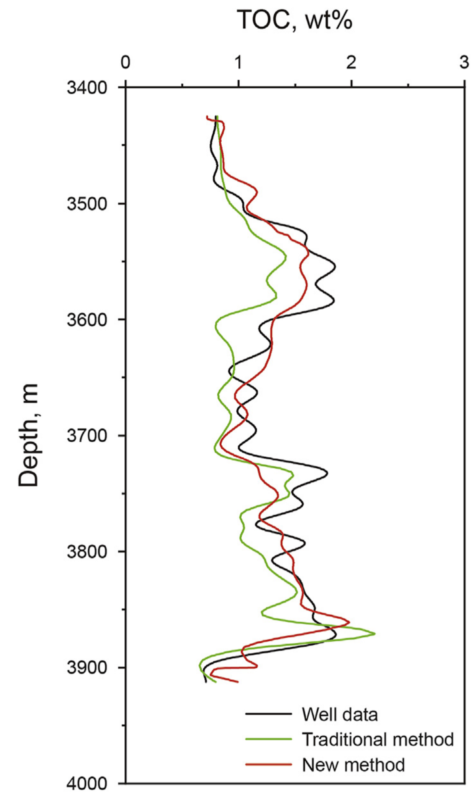

Fig. 25. Comparison of the calculated TOC and the predicted TOC, where the calculated TOC is in black, the predicted TOC by the proposed method is in red, and the predicted TOC by the traditional method is in green.

are isotropic, clay-rich, and with low maturity. In the future, we will focus on two aspects of the TOC seismic prediction. One is incorporating the maturity of organic matter to improve the applicability of the rock physics model. The other is extending the TOC prediction method proposed in this paper to shale, which will consider the anisotropic characteristic of shale.

Declaration of competing interest

No conflict of interest exits in the submission of this manuscript, and manuscript is approved by all authors for publication. I would like to declare on behalf of my coauthors that the work described was original research that has not been published previously, and not under consideration for publication elsewhere, in whole or in part.

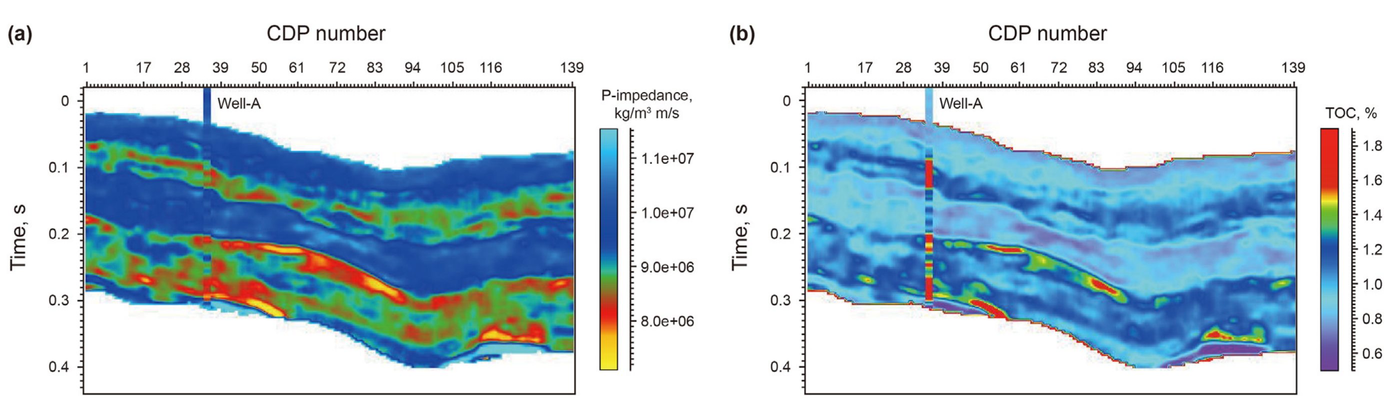

Fig. 24. Inversion results of the traditional prediction method on the same actual seismic profile, where (a) shows the P-wave impedance, (b) shows the converted TOC. The corresponding profiles of well-A are plotted for calibration.

All the authors listed have approved the manuscript that is enclosed.

Acknowledgements

The authors acknowledge the sponsorship of National Natural Science Foundation of China (42174139, 41974119, 42030103), Laoshan Laboratory Science and Technology Innovation Program (LSKJ202203406) and Science Foundation from Innovation and Technology Support Program for Young Scientists in Colleges of Shandong Province and Ministry of Science and Technology of China (2019RA2136).

Appendix A

The expressions of $T_{iijj}(\alpha_k)$ and $F(\alpha_k)$ in Eq. (10) and Eq (11)

Assuming that kerogen is spheroidal inclusion, the tensor $T_{iijj}(\alpha_k)$ and $F(\alpha_k)$ in the Kuster-Toksöz equations (Eq. (8) and Eq. (9)) are derived from a tensor T_{ijkl} that relates the uniform strain field at infinity to the strain field within an ellipsoidal elastic inclusion (Wu, 1966), Berryman (1980) gave the formulations for calculating $T_{iijj}(\alpha_k)$ and $F(\alpha_k)$, as follows:

$$T_{iijj}(\alpha_k) = \frac{3F_1}{F_2}, \tag{A-1}$$

and

$$F(\alpha_k) = \frac{2}{F_3} + \frac{1}{F_4} + \frac{F_4F_5 + F_6F_7 - F_8F_9}{F_2F_4}, \tag{A-2}$$

where

$$F_1 = 1 + A\left[\frac{3}{2}(g+\upsilon) - R\left(\frac{3}{2}g + \frac{5}{2}\upsilon - \frac{4}{3}\right)\right], \tag{A-3}$$

$$F_2 = 1 + A\left[1 + \frac{3}{2}(g+\upsilon) - \frac{R}{2}(3g+5\upsilon)\right] + B(3-4R) + \frac{A}{2}(A+3B)(3-4R)\left[g+\upsilon-R\left(g-\upsilon+2\upsilon^2\right)\right], \tag{A-4}$$

$$F_3 = 1 + \frac{A}{2}\left[R(2-\upsilon) + \frac{1+\alpha^2}{\alpha^2}g(R-1)\right], \tag{A-5}$$

$$F_4 = 1 + \frac{A}{4}[3\upsilon + g - R(g-\upsilon)], \tag{A-6}$$

$$F_5 = A\left[R\left(g+\upsilon-\frac{4}{3}\right) - g\right] + B\upsilon(3-4R), \tag{A-7}$$

$$F_6 = 1 + A[1+g-R(\upsilon+g)] + B(1-\upsilon)(4-4R), \tag{A-8}$$

$$F_7 = 2 + \frac{A}{4}[9\upsilon+3g-R(5\upsilon+3g)] + B\upsilon(3-4R), \tag{A-9}$$

$$F_8 = A\left[1-2R+\frac{g}{2}(R-1)+\frac{\upsilon}{3}(5R-3)\right] + B(1-\upsilon)(3-4R), \tag{A-10}$$

$$F_9 = A[g(R-1)-R\upsilon] + B\upsilon(3-4R), \tag{A-11}$$

$$A = \frac{\mu'}{\mu} - 1, \tag{A-12}$$

$$B = \frac{1}{3}\left(\frac{K'}{K} - \frac{\mu'}{\mu}\right), \tag{A-13}$$

$$R = \frac{3\mu}{3K+4\mu}, \tag{A-14}$$

$$g = \frac{\alpha_k^2}{1-\alpha_k^2}(3\upsilon-2), \tag{A-15}$$

$$\upsilon = \frac{\alpha_k}{\left(1-\alpha_k{}^2\right)^{3/2}}\left[\cos^{-1}(\alpha_k) - \alpha_k\sqrt{1-\alpha_k^2}\right]. \tag{A-16}$$

In Eqs. (A-12)-(A-14), K and K' are the bulk moduli of the inorganic rock and kerogen, respectively; μ and μ' denote the shear moduli of the inorganic rock and kerogen, respectively. In Eq. (15) and Eq. (16), α is the aspect ratio of the kerogen. For the source rocks at different maturity stages, the elastic moduli of kerogen (K' and μ') are assumed to be constants. When the elastic moduli of the inorganic rock (K and μ), the kerogen aspect ratio (α) and the Poisson's ratio of inorganic rock (σ) are given, the tensors T_{iijj} and F can be determined by Eqs. (A-1)-(A-16).

References

Aki, K., Richards, P.G., 1980. Quantitative Seismology: Theory and Methods. W.H. Freeman, San Francisco.
Alemie, W., Sacchi, M.D., 2011. High-resolution three-term AVO inversion by means of a Trivariate Cauchy probability distribution. Geophysics 76 (3), R43–R55. https://doi.org/10.1190/1.3554627.
Amato del Monte, A., Antonielli, E., De Tomasi, V., et al., 2018. Methods for source rock identification on seismic data: an example from the Tanezzuft Formation (Tunisia). Mar. Petrol. Geol. 91, 108–124. https://doi.org/10.1016/j.marpetgeo.2017.12.015.
Amosu, A., Imsalem, M., Sun, Y., 2021. Effective machine learning identification of TOC-rich zones in the Eagle Ford Shale. J. Appl. Geophys. 188, 104311. https://doi.org/10.1016/j.jappgeo.2021.104311.
Backus, G., 1962. Long-Wave Elastic Anisotropy produced by horizontal layering. J. Geophys. Res. 67 (11), 4427–4440. https://doi.org/10.1029/JZ067i011p04427.
Berryman, J.G., 1980. Long-wavelength propagation in composite elastic media II. Ellipsoidal inclusions. J. Acoust. Soc. Am. 68 (6), 1820–1831. https://doi.org/10.1121/1.385172.
Berryman, J.G., 1995. Mixture theories for rock properties. Rock physics phase relations: A handb phys. constants 3, 205–228.
Broadhead, M.K., Cheshire, S.G., Hayton, S., 2016. The effect of TOC on acoustic impedance for a Middle Eastern source rock. Lead. Edge 35 (3), 258–264. https://doi.org/10.1190/tle35030258.1.
Brown, R.J.S., Korringa, J., 1975. On the dependence of the elastic preoperties of a porous rock on the compressibility of the pore fluid. Geophysics 40 (4), 608–616. https://doi.org/10.1190/1.1440551.
Buland, A., Omre, H., 2003. Bayesian linearized AVO inversion. Geophysics 68 (1), 185–198. https://doi.org/10.1190/1.1543206.
Carcione, J.M., 2000. A model for seismic velocity and attenuation in petroleum source rocks. Geophysics 65 (4), 1080–1092. https://doi.org/10.1190/1.1444801.
Carcione, J.M., Avseth, P., 2015. Rock-physics templates for clay-rich source rocks. Geophysics 80 (5), D481–D500. https://doi.org/10.1190/geo2014-0510.1.
Carcione, J.M., Helle, H.B., Avseth, P., 2011. Source-rock seismic-velocity models: Gassmann versus Backus. Geophysics 76 (5), N37–N45. https://doi.org/10.1190/geo2010-0258.1.
Carmichael, R.S., 2017. Practical Handbook of Physical Properties of Rocks and Minerals. CRC press, 1988.
Chan, S.A., Hassan, A.M., Usman, M., et al., 2022. Total organic carbon (TOC) quantification using artificial neural networks: improved prediction by leveraging XRF data. J. Petrol. Sci. Eng. 208, 109302. https://doi.org/10.1016/j.petrol.2021.109302.
Ciz, R., Shapiro, S.A., 2009. Stress-dependent anisotropy in transversely isotropic rocks: comparison between theory and laboratory experiment on shale. Geophysics 74 (1), D7–D12. https://doi.org/10.1190/1.3008546.
Daubechies, I., DeVore, R., Fornasier, M., et al., 2010. Iteratively reweighted least squares minimization for sparse recovery. Commun. Pure Appl. Math. 63 (1), 1–38. https://doi.org/10.1002/cpa.20303.

Deng, J.X., Wang, H., Zhou, H., et al., 2015. Microtexture seismic rock physical properties and modeling of Longmaxi Formation shale. China Sea. Chin. J. Geophys. 58 (6), 2123–2136. https://doi.org/10.6038/cjg20150626 (in Chinese).

Ding, P.B., Gong, F., Zhang, F., et al., 2021. A physical model study of shale seismic responses and anisotropic inversion. Petrol. Sci. 18 (4), 1059–1068. https://doi.org/10.1016/j.petsci.2021.01.001.

Dong, N., Huo, Z.Z., Sun, Z.D., et al., 2014. An investigation of a new rock physics model for shale. Chin. J. Geophys. 57 (6), 1990–1998. https://doi.org/10.6038/cjg20140629 (in Chinese).

Downton, J., 2005. Seismic Parameter Estimation from AVO Inversion. University of Calgary.

Fu, B.Y., Fu, L.Y., Cao, C.H., et al., 2020. The analysis of the influence of organic content on the ealstic properties of shale based on solid substitution model. Chin. J. Geophys. 63 (7), 2823–2835. https://doi.org/10.6038/cjg2020N0039 (in Chinese).

Gassmann, F., 1951. Elastic waves through a packing of spheres. Geophysics 16 (4), 673–685. https://doi.org/10.1190/1.1437718.

Gidlow, P.M., Smith, G.C., Vail, P., 1993. Hydrocarbon detection using fluid factor traces: a case study, 3rd SAGA biennial conference and exhibition. Eur. Assoc. Geoscientists Eng. https://doi.org/10.3997/2214-4609-pdb.224.041.

Grana, D., 2016. Bayesian linearized rock-physics inversion. Geophysics 81 (6), D625–D641. https://doi.org/10.1190/geo2016-0161.1.

Gray, D., Goodway, B., Chen, T., 1999. Bridging the gap: using AVO to detect changes in fundamental elastic constants, SEG Technical Program Expanded Abstracts 1999. Soc. Explor. Geophys. 852–855. https://doi.org/10.1190/1.1821163.

Gui, J.C., Ma, T.S., Chen, P., 2020. Rock physics modeling of transversely isotropic shale: an example of the Longmaxi formation in the Sichuan basin. Chin. J. Geophys. 63 (11), 4188–4204. https://doi.org/10.6038/cjg2020N0294 (in Chinese).

Han, X., Nie, J., Guo, J., et al., 2019. Rock physics modelling of elastic properties of organic shale considering kerogen stress and pore pressure distribution. J. Petrol. Sci. Eng. 174, 891–902. https://doi.org/10.1016/j.petrol.2018.11.063.

Hansen, J.A., Mondol, N.H., Fawad, M., 2019. Organic content and maturation effects on elastic properties of source rock shales in the Central North Sea. Interpretation 7 (2), T477–T497. https://doi.org/10.1190/INT-2018-0105.1.

Herron, S.L., 1987. A total organic carbon log for source rock evaluation. Log. Anal. 28 (6).

Hill, R., 1952. The elastic behaviour of a crystalline aggregate. Phys. Soc. Sect. A. 65 (5), 349.

Hornby, B.E., Schwartz, L.M., Hudson, J.A., 1994. Anisotropic effective-medium modeling of the elastic properties of shales. Geophysics 59 (10), 1570–1583. https://doi.org/10.1190/1.1443546.

Keys, R.G., Xu, S., 2002. An approximation for the Xu-White velocity model. Geophysics 67 (5), 1406–1414. https://doi.org/10.1190/1.1512786.

Kuster, G.T., Toksöz, M.N., 1974. Velocity and attenuation of seismic waves in two-phase media: Part I. Theoretical formulations. Geophysics 39 (5), 587–606. https://doi.org/10.1190/1.1440450.

Li, K., Yin, X.Y., Zong, Z.Y., et al., 2020. Seismic AVO statistical inversion incorporating poroelasticity. Petrol. Sci. 17 (5), 1237–1258. https://doi.org/10.1007/s12182-020-00483-5.

Li, Q.W., Pang, X.Q., Li, B.Y., et al., 2018. Discrimination of effective source rocks and evaluation of the hydrocarbon resource potential in Marsel. Kazakhstan. J. Petrol. Sci. Eng. 160, 194–206. https://doi.org/10.1016/j.petrol.2017.10.029.

Li, Y., Guo, Z.Q., Liu, C., et al., 2015. A rock physics model for the characterization of organic-rich shale from elastic properties. Petrol. Sci. 12 (2), 264–272. https://doi.org/10.1007/s12182-015-0029-6.

Løseth, H., Wensaas, L., Gading, M., et al., 2011. Can hydrocarbon source rocks be identified on seismic data? Geology 39 (12), 1167–1170. https://doi.org/10.1130/G32328.1.

Mavko, G., Mukerji, T., Dvorkin, J., 2009. The Rock Physics Handbook: Tools for Seismic Analysis of Porous Media. Cambridge University Press, Cambridge.

Sahoo, T.R., Funnell, R.H., Brennan, S.W., et al., 2021. Delineation of coaly source rock distribution and prediction of organic richness from integrated analysis of seismic and well data. Mar. Petrol. Geol. 125, 104873. https://doi.org/10.1016/j.marpetgeo.2020.104873.

Saxena, N., Mavko, G., 2014. Exact equations for fluid and solid substitution. Geophysics 79 (3), L21–L32. https://doi.org/10.1190/geo2013-0187.1.

Sayers, C.M., 2013. The effect of kerogen on the elastic anisotropy of organic-rich shales. Geophysics 78 (2), D65–D74. https://doi.org/10.1190/geo2012-0309.1.

Shalaby, M.R., Jumat, N., Lai, D., et al., 2019. Integrated TOC prediction and source rock characterization using machine learning, well logs and geochemical analysis: case study from the Jurassic source rocks in Shams Field, NW Desert, Egypt. J. Petrol. Sci. Eng. 176, 369–380. https://doi.org/10.1016/j.petrol.2019.01.055.

Suwannasri, K., Vanorio, T., Clark, A., 2018. Monitoring the changes in the microstructure and the elastic and transport properties of Eagle Ford marl during maturation. Geophysics 83 (5), MR263–MR281. https://doi.org/10.1190/geo2017-0797.1.

Tissot, B., Durand, B., Espitalié, J., et al., 1974. Influence of nature and diagenesis of organic matter in formation of petroleum. AAPG Bull. 58 (3), 499–506. https://doi.org/10.1306/83D91425-16C7-11D7-8645000102C1865D.

Tosaya, C., Nur, A., 1982. Effects of diagenesis and clays on compressional velocities in rocks. Geophys. Res. Lett. 9 (1), 5–8. https://doi.org/10.1029/GL009i001p00005.

Vernik, L., Landis, C., 1996. Elastic anisotropy of source rocks: implications for hydrocarbon generation and primary migration. AAPG Bull. 80 (4), 531–544. https://doi.org/10.1306/64ED8836-1724-11D7-8645000102C1865D.

Vernik, L., Liu, X., 1997. Velocity anisotropy in shales: a petrophysical study. Geophysics 62 (2), 521–532. https://doi.org/10.1190/1.1444162.

Vernik, L., Nur, A., 1992. Ultrasonic velocity and anisotropy of hydrocarbon source rocks. Geophysics 57 (5), 727–735. https://doi.org/10.1190/1.1443286.

Wang, Y.R., Zong, Z.Y., Yin, X.Y., 2022. Fluid discrimination incorporating amplitude variation with angle inversion and squirt flow of the fluid. Petrol. Sci. 19 (4), 1592–1604. https://doi.org/10.1016/j.petsci.2022.03.007.

Wood, A.W., 1955. A Textbook of Sound. The MacMillan Co., New Tork.

Wu, T.T., 1966. The effect of inclusion shape on the elastic moduli of a two-phase material. Int. J. Solid Struct. 2 (1), 1–8. https://doi.org/10.1016/0020-7683(66)90002-3.

Xu, S., Payne, M.A., 2009. Modeling elastic properties in carbonate rocks. Lead. Edge 28 (1), 66–74. https://doi.org/10.1190/1.3064148.

Xu, S., White, R.E., 1995. A new velocity model for clay-sand mixtures. Geophys. Prospect. 43, 91–118. https://doi.org/10.1111/j.1365-2478.1995.tb00126.x.

Yin, L., Yin, X., Zong, Z., et al., 2020. A new rock physics model method for shale on the theory of micro-nanopores. Chin. J. Geophys. 63 (4), 1642–1653. https://doi.org/10.6038/cjg2020M0448 (in Chinese).

Yu, S., Zong, Z., Yin, X., 2021. Rock physical model and AVO patterns for the mud-rich source rock. Front. Earth Sci. 9. https://doi.org/10.3389/feart.2021.633930.

Zargari, S., Canter, K.L., Prasad, M., 2015. Porosity evolution in oil-prone source rocks. Fuel 153, 110–117. https://doi.org/10.1016/j.fuel.2015.02.072.

Zhang, Y.Y., He, Z.L., Jiang, S., et al., 2018. Controls on the organic carbon content of the lower Cambrian black shale in the southeastern margin of Upper Yangtze. Petrol. Sci. 15 (4), 709–721. https://doi.org/10.1007/s12182-018-0262-x.

Zhao, L.X., Qin, X., Han, D.H., et al., 2016. Rock-physics modeling for the elastic properties of organic shale at different maturity stages. Geophysics 81 (5), D527–D541. https://doi.org/10.1190/geo2015-0713.1.

Zhao, L.X., Liu, J.S., Yao, Y.X., et al., 2021. Quantitative seismic characterization of source rocks in lacustrine depositional setting using the Random Forest method: an example from the Changjiang sag in East China Sea basin. Chin. J. Geophys. 64 (2), 700–715. https://doi.org/10.6038/cjg2021O0123 (in Chinese).

Zoeppritz, K., 1919. On the reflection and propagation of seismic waves. Göttinger Nachr. 1 (5), 66–84.

Zong, Z.Y., Feng, Y.W., Yin, X.Y., et al., 2021. Fluid discrimination incorporating viscoelasticity and frequency-dependent amplitude variation with offsets inversion. Petrol. Sci. 18 (4), 1047–1058. https://doi.org/10.1016/j.petsci.2020.10.001.

Zong, Z., Ji, L., 2020. Model parameterization and amplitude variation with angle and azimuthal inversion in orthotropic media. Geophysics 86 (1), R1–R14. https://doi.org/10.1190/geo2018-0778.1.

Zong, Z., Sun, Q., 2022. Density stability estimation method from pre-stack seismic data. J. Petrol. Sci. Eng. 208, 109373. https://doi.org/10.1016/j.petrol.2021.109373.

Zong, Z., Yin, X., 2016. Direct inversion of Young's and Poisson impedances for fluid discrimination. Geofluids 16 (5), 1006–1016. https://doi.org/10.1111/gfl.12202.

Zong, Z., Yin, X., 2017. Model parameterization and P-wave AVA direct inversion for Young's impedance. Pure Appl. Geophys. 174 (5), 1965–1981. https://doi.org/10.1007/s00024-017-1529-7.

Zong, Z., Yin, X., Wu, G., 2015. Geofluid discrimination incorporating poroelasticity and seismic reflection inversion. Surv. Geophys. 36 (5), 659–681. https://doi.org/10.1007/s10712-015-9330-6.